Supporting Material

Direct Calculation of Protein Fitness Landscapes through Computational Protein Design

L. Au and D. F. Green, 2015

Note: Residue positions in all figures are listed alpha-numerically with the protein chain (A, B, and G for the α-, β- and γ-subunits, respectively), followed by the position number according to the PDB file, and a single-letter code for the wild-type amino acid. Histidine states may be singly protonated at δ- or ε-nitrogens and are listed with lower-case 'd' (or Hδ) and 'e' (or Hε), respectively; when it is doubly protonated, we indicate this with lower-case 'p' or with H+.

List of Figures

S1 Implementation of DEE/A* protocol . . . 4
S2 Removing sequences to determine neutrality . . . 5
S3 Effect of changing ε_{cut} in defining neutrality . . . 5
S4 Structural examples for calibrating effective energy . . . 6
S5 Gα mutations: stability relative to wild type, $\langle\Delta\Delta G_{fold}\rangle$ . . . 9
S6 G$\beta\gamma$-heterodimer: stability relative to wild type, $\langle\Delta\Delta G_{fold}\rangle$ . . . 10
S7 Gα mutations: binding relative to wild type, $\langle\Delta\Delta G_{bind}\rangle$ . . . 11
S8 G$\beta\gamma$-heterodimer: binding relative to wild type, $\langle\Delta\Delta G_{bind}\rangle$ . . . 12
S9 Residues at Gα–G$\beta\gamma$ binding interface . . . 13
S10 Gα-subunit: $\max(\langle\Delta\Delta G_{fold}\rangle, \langle\Delta\Delta G_{bind}\rangle)$ . . . 14
S11 G$\beta\gamma$-heterodimer: $\max(\langle\Delta\Delta G_{fold}\rangle, \langle\Delta\Delta G_{bind}\rangle)$ . . . 15
S12 Distribution of unconverged states . . . 17
S13 Convergence in Gα, $\langle\Delta\Delta G_{fold}\rangle$ . . . 18
S14 Convergence in G$\beta\gamma$, $\langle\Delta\Delta G_{fold}\rangle$ . . . 19
S15 Correlation between energy minimization and DEE/A* . . . 20
S16 Energetic differences between DEE/A* and minimization . . . 20
S17 Disparity between DEE/A* and minimization routines . . . 21
S18 Amino-acid frequency of occurrence for wild-type heterotrimer. . . . 23
S19 DEE/A* and PAM120 e_{ij} values. . . . 24
S20 DEE/A* and BLOSUM62 e_{ij} values . . . 25
S21 Randomized matrices and DEE/A* . . . 26
S22 Comparing substitution rates between random samples and DEE/A* . . . 27
S23 Correlation between DEE/A* and thermal stability for alanine scanning . . . 29
S24 Proportion of positive and negative outcomes in alanine scanning . . . 30
S25 Computed p-values for all positions . . . 33

List of Tables

S1 Salt bridge: GαD20–GβR52, $\Delta\Delta G_{bind}$ mutations 6
S2 Salt bridge: GαE216–GβK57, $\Delta\Delta G_{bind}$ mutations 6
S3 Hydrogen-bond network: GβR68–GβD83–GβT86, $\Delta\Delta G_{bind}$ mutations . . . 7
S4 Intervals for conformational subsets 16
S5 Comparison of DEE/A* and random data 27
S6 Comparing permuted and original matrices 28
S7 Contingency table: DEE/A* comparison with thermal stability 29
S8 Contingency table: randomized DEE/A* compared with thermal stability. . 30
S9 List of point mutations for Gβ 32
S10 List of positions with known binding interactions. 34
S11 List of positions predicted to make significant binding contributions 35

1 Overview of computational protocol

A molecular dynamics simulation was performed on $G\alpha_{i1}\beta_1\gamma_2$, and protein conformations were taken from 50-ns intervals over a 350-ns trajectory; a total of 40 snapshots were used in our analysis (5 conformations from each interval,) as shown in **Fig. S1**. Every position in a given protein conformation is mutated to each of the naturally occurring amino acids, except proline and glycine, and the rotamers that are incompatible with a low-energy conformation for a given sequence are discarded. From the remaining rotamer choices, the global minimum energy conformation and additional structures within a designated energy cutoff from it are identified. We have chosen a 30-kcal/mol cutoff for this, and have found that over 90% of all possible single-site mutations satisfy this constraint.

2 Neutral mutations defined by energetic landscape

Neutral mutations, those that neither worsen nor improve fitness, were defined based on the distribution of $\Delta\Delta G_{fold}$ and $\Delta\Delta G_{bind}$ on the energy landscape, after referencing to the wild-type sequence; the proportion of mutant sequences was highest around the origin, suggesting that most mutations have a neutral effect. Sequences simultaneously sharing $\Delta\Delta G_{fold}$ and $\Delta\Delta G_{bind}$ within a designated energy cutoff, ε_{cut}, were removed from the data set (e.g. $|\Delta\Delta G_{fold}| \leq \varepsilon_{cut}$ and $|\Delta\Delta G_{bind}| \leq \varepsilon_{cut}$) (**Fig. S2**). The proportion of remaining sequences was calculated for various energy cutoffs, and compared. At the 1.5-kcal/mol cutoff, a significant reduction in sequence space is observed, and thus taken as the energetic cutoff for defining neutrality (**Fig. S3**).

3 Effective temperature for DEE/A*

A Boltzmann-weighted average was computed for each mutation over all 40 snapshots, and an effective temperature for the distribution is necessary to rescale computed results so that the values could better reflect energetic changes due to conformational entropy. A number of temperatures were tested to gauge the compatibility between structures found and their computed energies; we focused on energetic changes after mutation at salt-bridges and hydrogen bonds to set a baseline (**Fig. S4**).

Most hydrogen bonds, involving nitrogen and oxygen, are expected to have ∼2–7 kcal/mol each, and we used this as a guideline to compare our calculations for specific mutations at different temperatures (**Tables S1**–**S3**). Our goal was to identify a temperature at which the loss or gain of hydrogen bonds would fall within the 2–7 kcal/mol interval, and the lowest energy that achieves this is at 4500K.

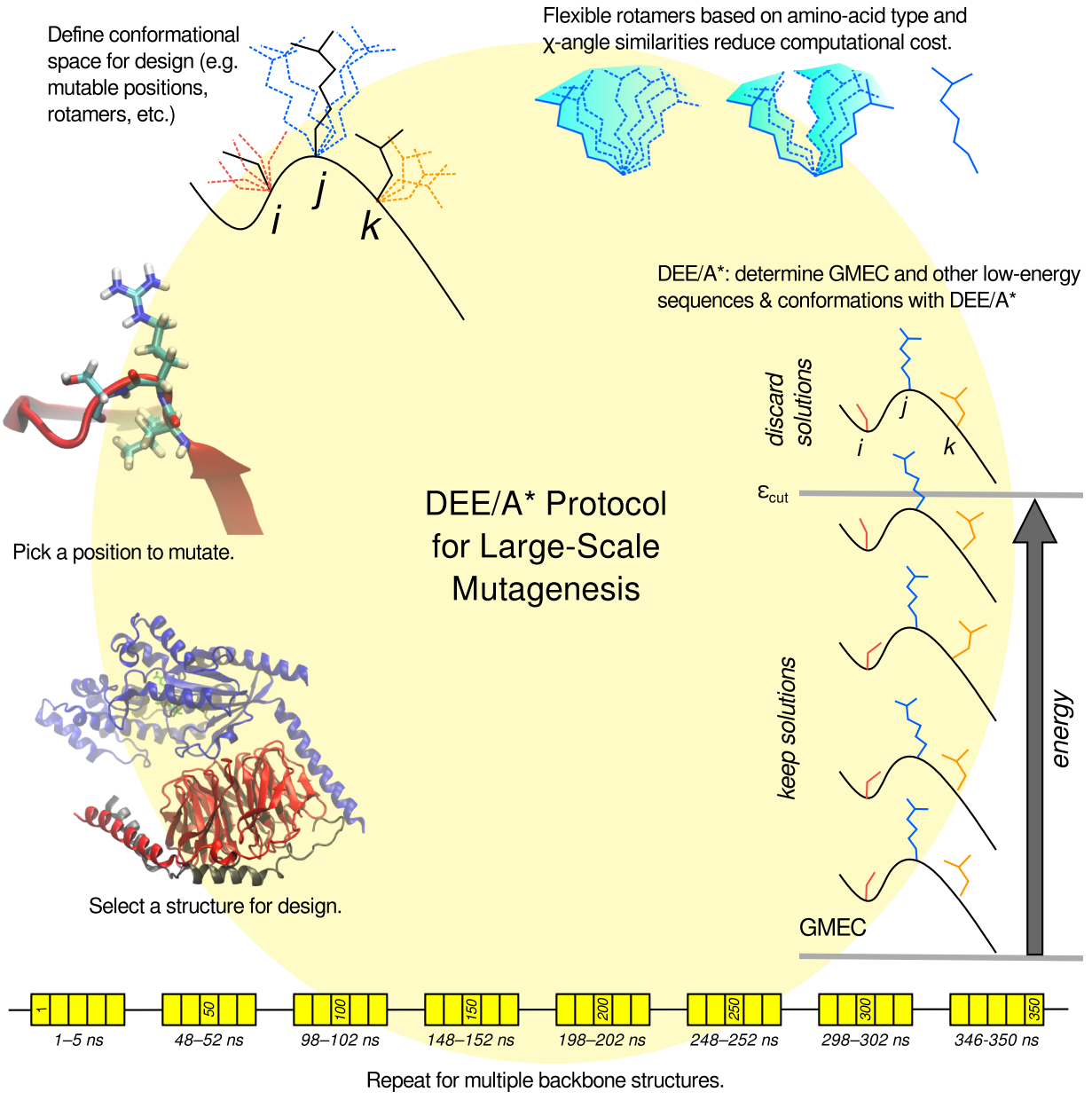

Figure S1: (Main-text figure 1b.) Representative protein backbones are mutated systematically until low-energy sequences within ε_{cut} and their corresponding conformations are found.

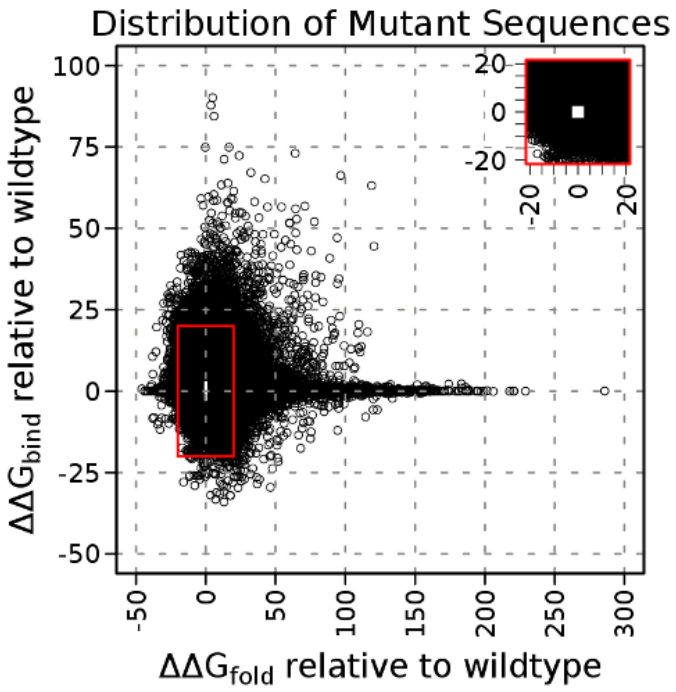

Figure S2: Sequences within 1.5 kcal/mol of $\Delta\Delta G_{fold}$ and $\Delta\Delta G_{bind}$, based on absolute value, removed.

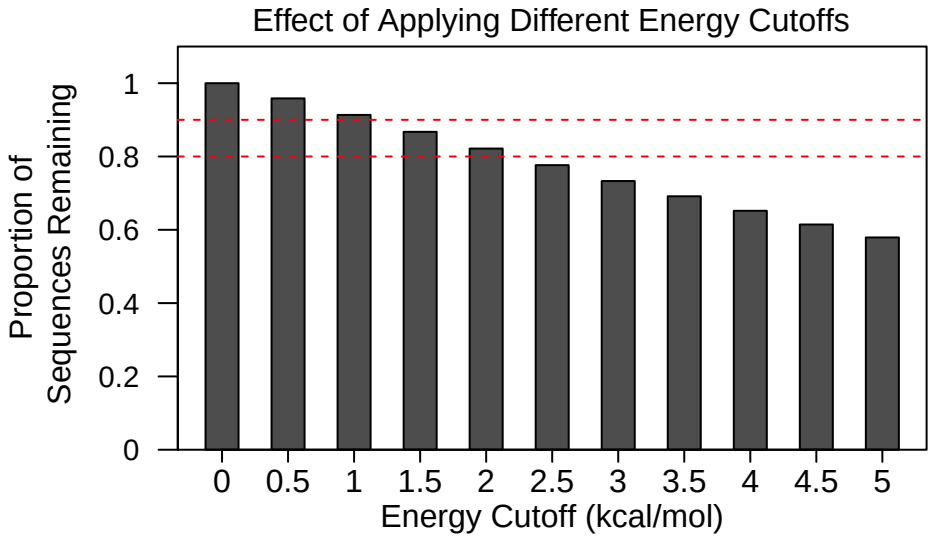

Figure S3: The proportion of sequences remaining after removing neutral sequences, defined by different ε_{cut}, is shown.

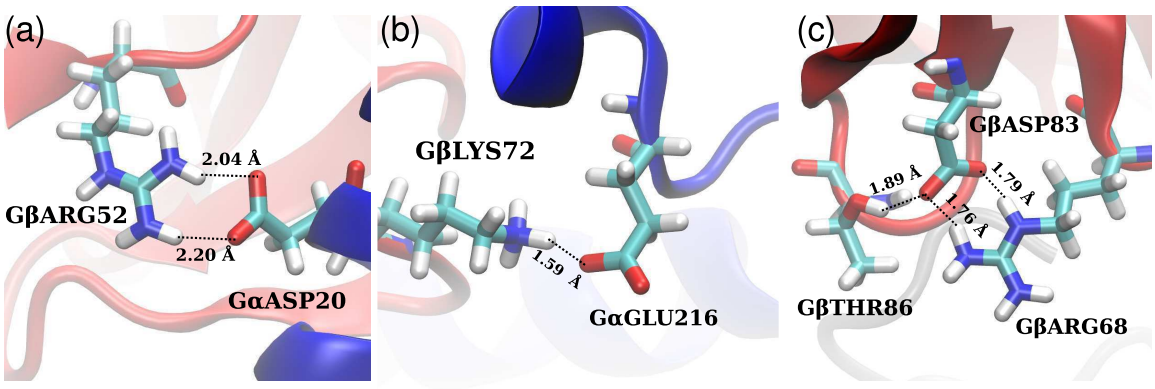

Figure S4: Temperature for effective energy was based on well-established intermolecular interactions: (a) doubly-bonded salt bridge, GαD20–GβR52, (b) singly-bonded salt bridge, GαE216–GβK57, and (c) a hydrogen-bond network between GβR68–GβE83–GβT86

Table S1: $\langle \Delta\Delta G_{bind} \rangle$ in kcal/mol for select mutations at GαD20–GβR52 salt bridge.

Temp. (K)	GαD20A	GαD20E	GαD20N	GαD20Q	GβR52A	GβR52K
300	-1.5± 0.2	-13.1 ± 2.0	-4.8 ± 0.7	-7.2 ± 0.9	5.2 ± 1.0	0.0 ± 0.0
1500	-0.2 ± 0.1	-10.4 ± 1.0	-2.9 ± 0.4	-5.6 ± 0.5	1.8 ± 0.4	1.3 ± 0.1
3000	2.1 ± 0.1	-6.7 ± 0.5	0.4 ± 0.2	-2.6 ± 0.3	2.2 ± 0.2	1.8 ± 0.1
4500	3.3 ± 0.1	-4.6 ± 0.3	1.9 ± 0.2	-1.1 ± 0.2	2.4 ± 0.1	2.0 ± 0.1
6000	4.0 ± 0.2	-3.5 ± 0.3	2.7 ± 0.2	-0.3 ± 0.2	2.6 ± 0.1	2.2 ± 0.1
9000	4.9 ± 0.2	-2.4 ± 0.2	3.6 ± 0.2	0.7 ± 0.2	2.7 ± 0.1	2.5 ± 0.1
300,000	7.7 ± 0.3	0.3 ± 0.3	6.3 ± 0.3	3.3 ± 0.3	3.0 ± 0.1	3.2 ± 0.1

Table S2: $\langle \Delta\Delta G_{bind} \rangle$ in kcal/mol for select mutations at GαE216–GβK57 salt bridge.

Temp. (K)	Gα E216A	Gα E216D	Gα E216N	Gα E216Q	Gβ K57A	Gβ K57R
300	2.0 ± 0.3	-2.6 ± 0.4	-8.7 ± 1.4	-7.6 ± 1.1	-8.0 ± 1.3	-10.2 ± 1.6
1500	1.2 ± 0.3	-0.7 ± 0.1	-4.5 ± 0.7	-7.0 ± 0.5	-8.0 ± 1.3	-10.2 ± 1.6
3000	1.1 ± 0.2	1.3 ± 0.1	-1.5 ± 0.3	-5.0 ± 0.2	-7.9 ± 1.3	-10.0 ± 1.6
4500	1.9 ± 0.1	2.3 ± 0.1	-0.2 ± 0.2	-4.2 ± 0.2	-6.4 ± 1.1	-7.8 ± 1.3
6000	2.4 ± 0.1	2.8 ± 0.1	0.5 ± 0.2	-3.8 ± 0.1	-3.1 ± 0.8	-4.4 ± 0.9
9000	2.9 ± 0.1	3.3 ± 0.1	1.2 ± 0.1	-3.3 ± 0.1	2.3 ± 0.4	-0.3 ± 0.4
300,000	3.9 ± 0.1	4.4 ± 0.1	2.4 ± 0.1	-2.5 ± 0.1	8.0 ± 0.1	4.6 ± 0.2

Table S3: $\langle \Delta\Delta G_{bind} \rangle$ for select mutations in the hydrogen-bond network

Temp. (K)	Gβ R68A	Gβ R68K		
300	9.3 ± 1.3	-2.9 ± 0.4		
1500	3.7 ± 0.4	-1.4 ± 0.3		
3000	3.1 ± 0.2	-0.1 ± 0.2		
4500	3.2 ± 0.2	0.6 ± 0.1		
6000	3.3 ± 0.2	1.0 ± 0.1		
9000	3.4 ± 0.2	1.4 ± 0.1		
300,000	3.8 ± 0.1	2.3 ± 0.1		
	Gβ D83A	Gβ D83E	Gβ D83N	Gβ D83Q
300	-5.3 ± 0.9	-1.5 ± 0.2	-4.3 ± 0.7	-5.3 ± 0.8
1500	-4.3 ± 0.6	2.8 ± 0.3	-3.2 ± 0.4	-3.1 ± 0.6
3000	-1.8 ± 0.3	4.2 ± 0.2	-1.4 ± 0.3	-1.0 ± 0.3
4500	-0.1 ± 0.2	4.8 ± 0.2	0.0 ± 0.2	0.3 ± 0.2
6000	0.8 ± 0.2	5.1 ± 0.2	0.9 ± 0.1	1.0 ± 0.2
9000	1.8 ± 0.1	5.7 ± 0.2	1.9 ± 0.1	1.9 ± 0.2
300,000	3.5 ± 0.2	7.1 ± 0.2	4.0 ± 0.2	3.8 ± 0.2
	Gβ T86A	Gβ T86S	Gβ T86C	
300	-3.1 ± 0.5	-2.1 ± 0.3	-3.0 ± 0.3	
1500	-1.1 ± 0.2	-0.5 ± 0.1	-2.2 ± 0.2	
3000	0.3 ± 0.1	0.1 ± 0.1	-0.9 ± 0.1	
4500	0.9 ± 0.1	0.3 ± 0.1	-0.3 ± 0.1	
6000	1.2 ± 0.1	0.5 ± 0.1	0.0 ± 0.1	
9000	1.5 ± 0.1	0.8 ± 0.1	0.4 ± 0.1	
300,000	2.5 ± 0.1	1.9 ± 0.1	1.4 ± 0.1	

4 Complete mutation profiles for G$\alpha_{i1}\beta_1\gamma_2$

For each mutant sequence, the energetic difference relative to wild type is computed over an ensemble of states using backbone structures from the 40 chosen conformations, and an effective temperature of 4500 K was used to compute a Boltzmann-weighted average over them for each sequence. Energy profiles for each subunit of the heterotrimer were compiled to identify regions of high and low mutational sensitivity. These energetic changes due to mutation are shown with secondary structure for:

- Stability ($\langle\Delta\Delta G_{fold}\rangle$) of G$\alpha$ in context of a complete heterotrimer (**Fig. S5**).
- Stability ($\langle\Delta\Delta G_{bind}\rangle$) of $\beta\gamma$-heterodimer in context of a complete heterotrimer (**Fig. S6**).
- Binding interactions ($\langle\Delta\Delta G_{bind}\rangle$) of G$\alpha$ to $\beta\gamma$-heterodimer (**Fig. S7**).
- Binding interactions ($\langle\Delta\Delta G_{bind}\rangle$) of $\beta\gamma$ to the α subunit (**Fig. S8**).
- Residues involved in binding that show significant energetic variation (**Fig. S9**).
- Maximum of either stability or binding in each Gα mutant (**Fig. S10**).
- Maximum of either stability or binding in each $\beta\gamma$-heterodimer mutant (**Fig. S11**).

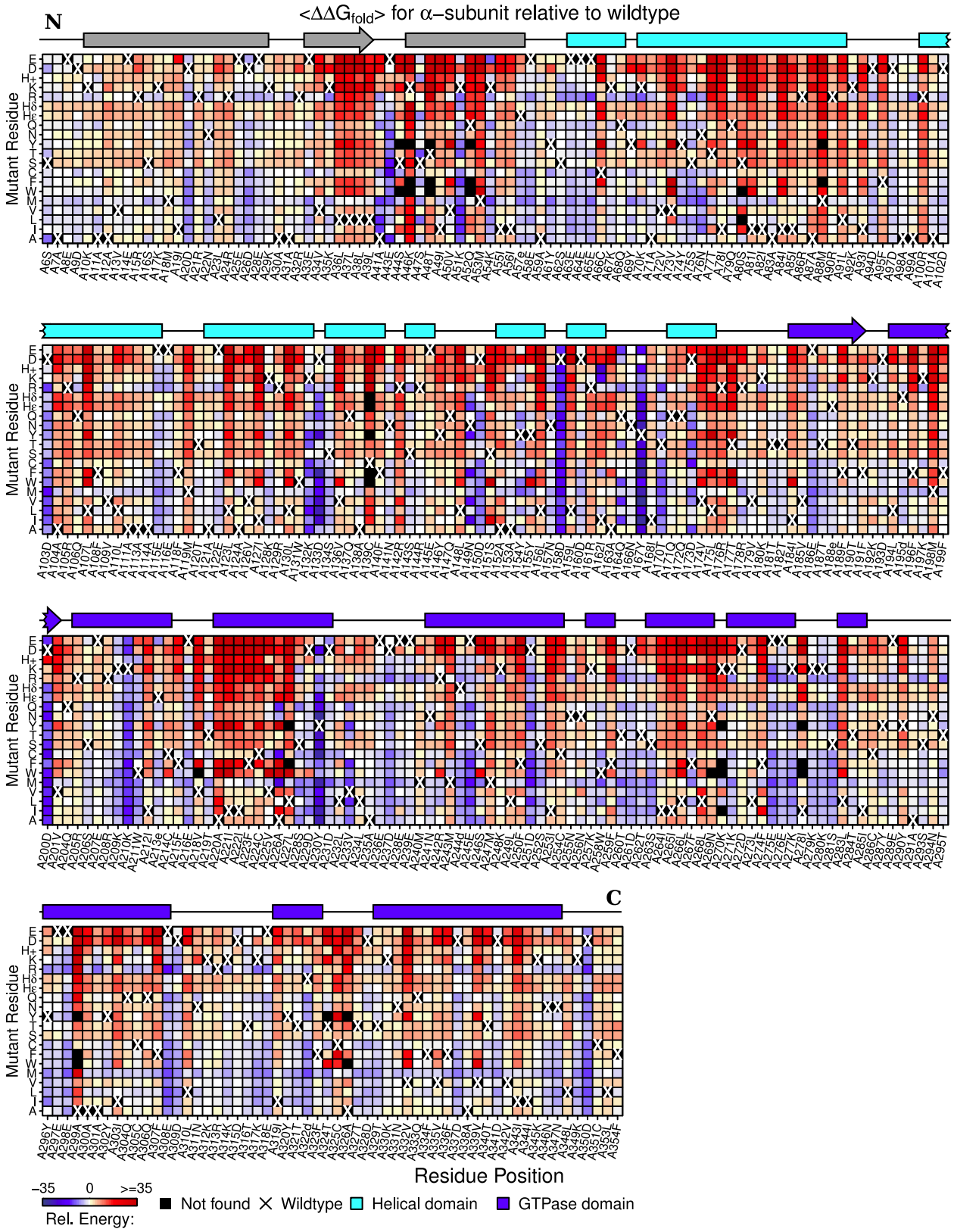

Figure S5: Stability ($\langle \Delta\Delta G_{fold} \rangle$) of G$\alpha$ sequences are organized according to position in the subunit and mutations are arranged according to amino-acid properties. The energy of each mutant (in kcal/mol) is referenced to the wild-type structure prior to averaging over the ensemble of states.

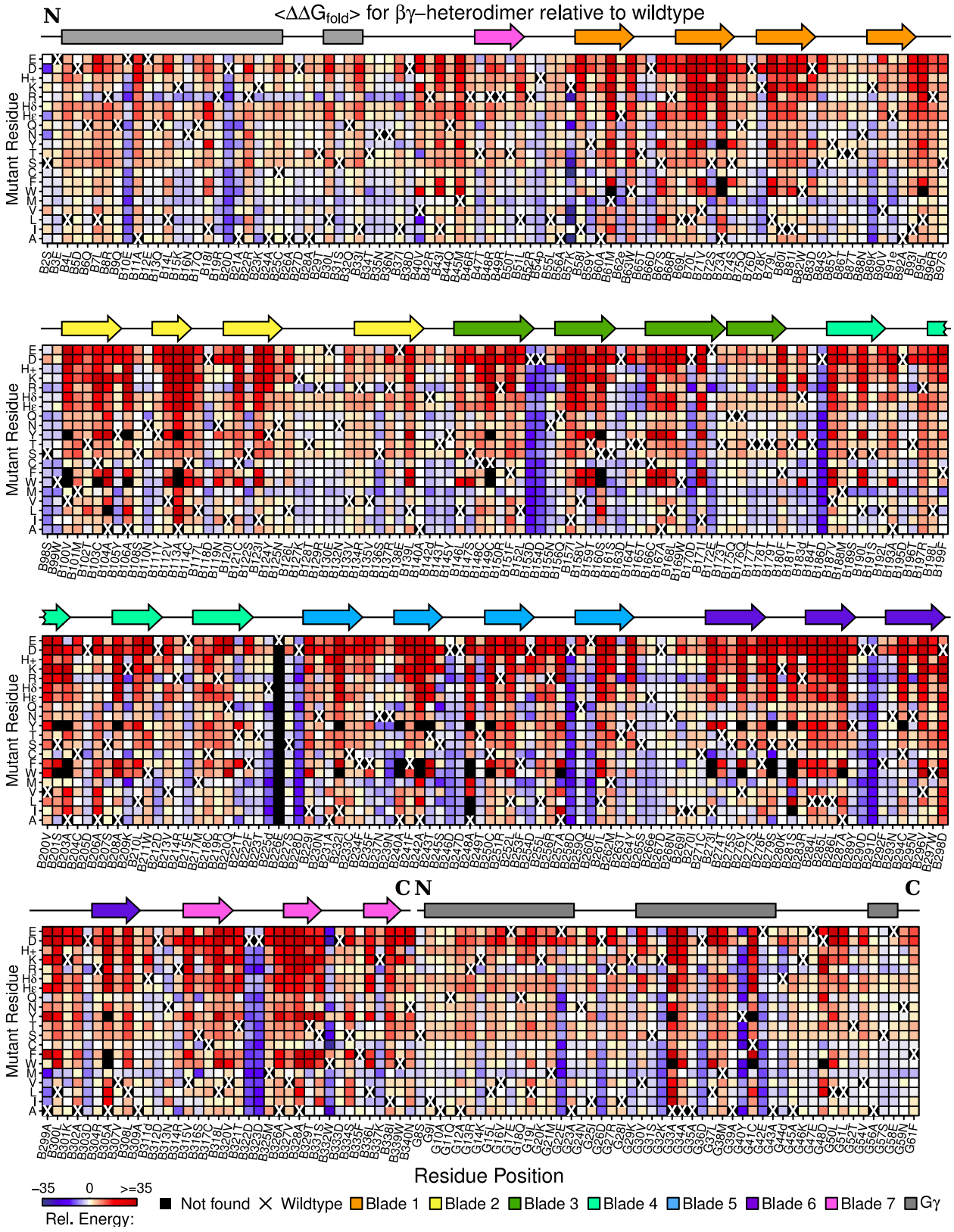

Figure S6: Stability ($\langle \Delta\Delta G_{fold} \rangle$) for the complete heterodimer is separated according to protein chain: Gβ is organized in repeating propeller blades, indicated by secondary structure illustrations, and Gγ follows. Wild-type amino acids are distinguished from mutations for reference, and mutant amino acids are ordered according to side-chain properties; favorable (blue) and unfavorable substitutions (red) can be identified quickly from this subset of protein sequence space.

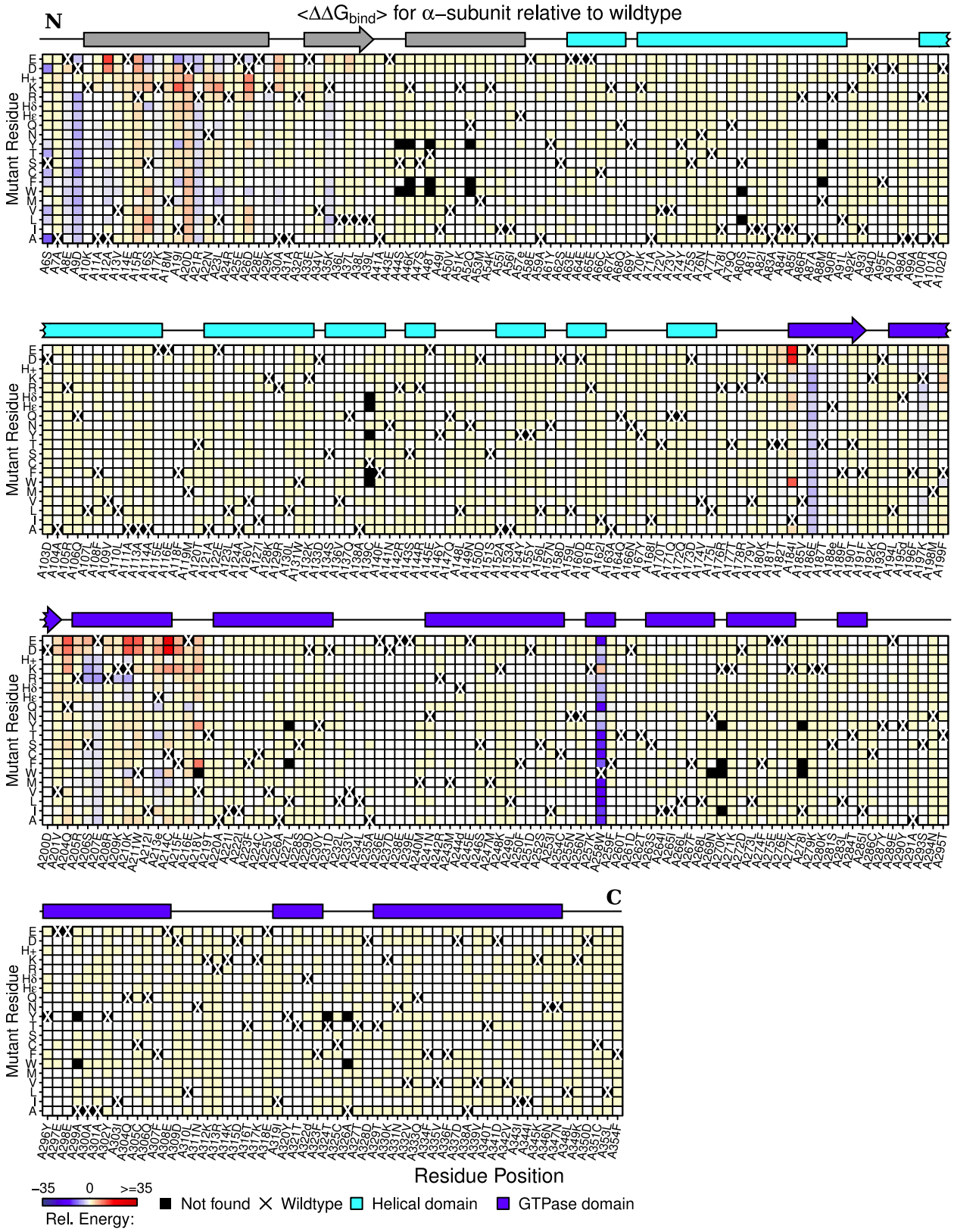

Figure S7: Average energy referenced to wild type is shown here for $\Delta\Delta G_{bind}$ for the α-subunit, based on how it binds to the $\beta\gamma$-heterodimer. Most mutations have a neutral effect, hence the profile is largely dominated by yellow tones.

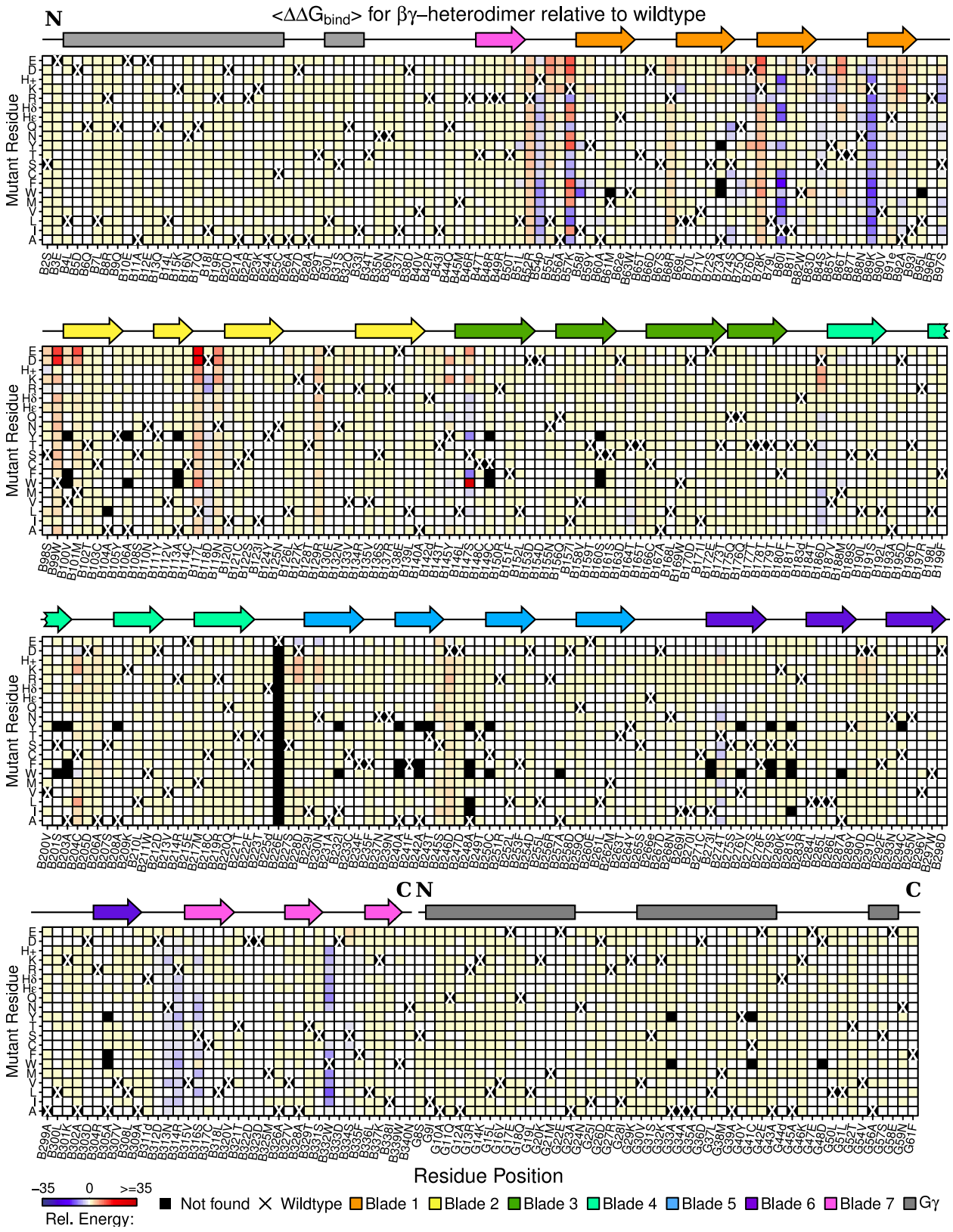

Figure S8: Average energy referenced to wild type is shown here for $\Delta\Delta G_{bind}$ for the $\beta\gamma$-heterodimer, based on its binding interactions with Gα. Most mutations have a neutral effect, as indicated by the yellow tones.

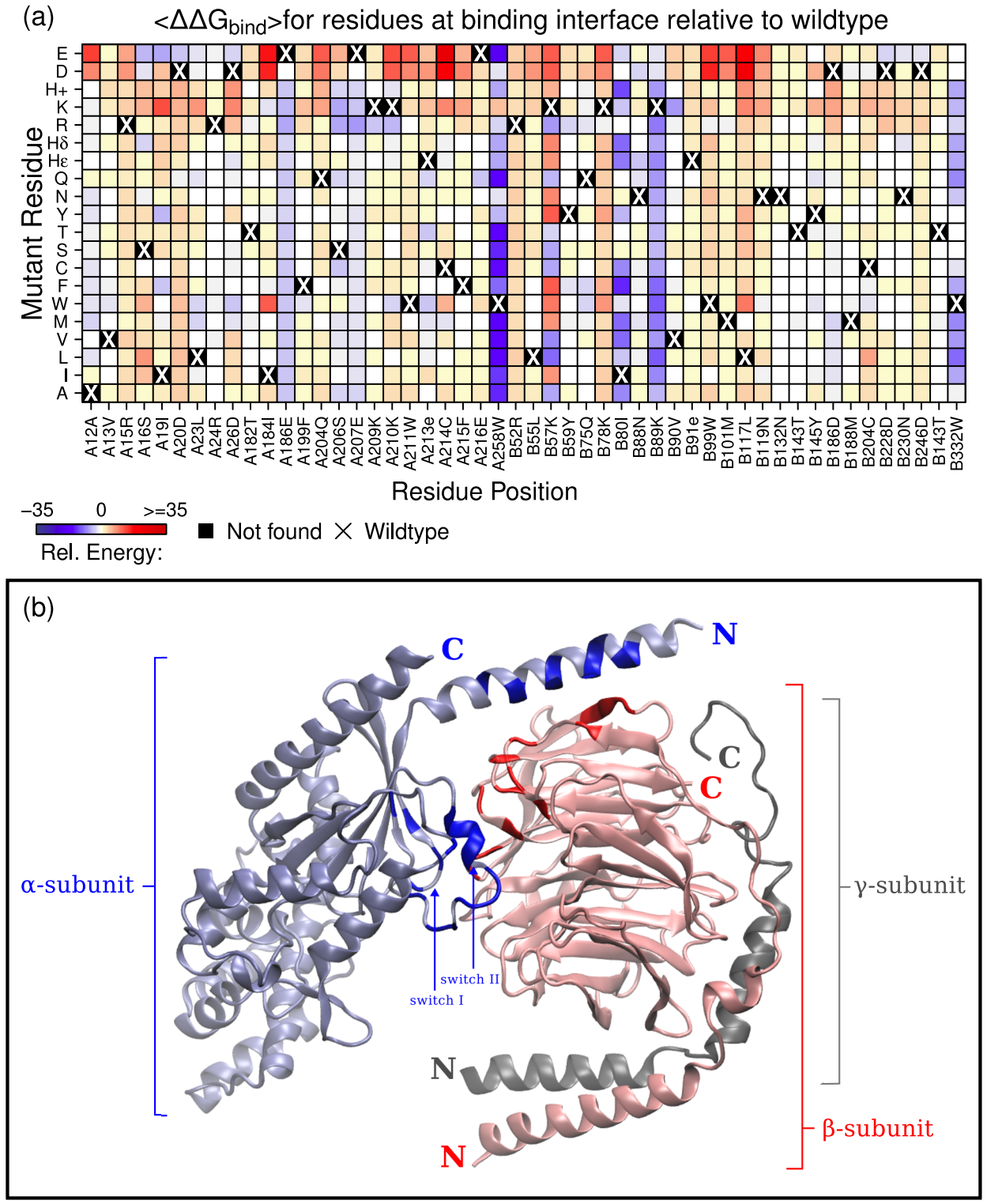

Figure S9: Most positions show no change in binding energy after mutation. (a) Here, the subset of positions with noticeable energetic variation are shown. (b) Structurally, these positions correspond well with the switch II region and amino terminus of Gα, both of which are known to bind with the $\beta\gamma$-heterodimer. Residues involved in binding according to (a) are shown in blue or red, superimposed onto the light blue-gray and light red subunits of the heterotrimer.

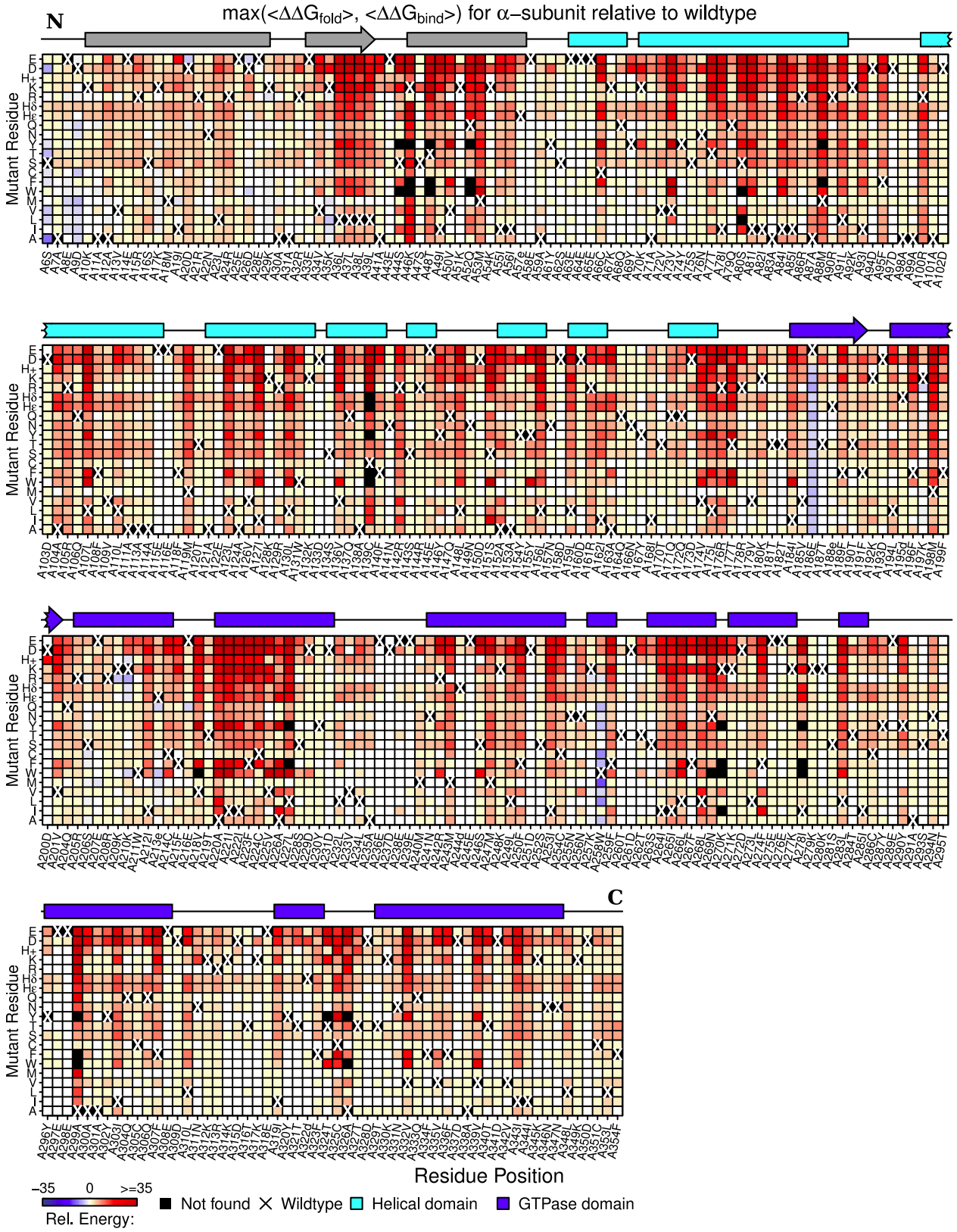

Figure S10: Proteins must stably fold and also bind to interaction partners. Here, the maximum energy of either term is shown; most worst-case scenario mutations are either neutral or unfavorable, as seen in yellow and red, respectively.

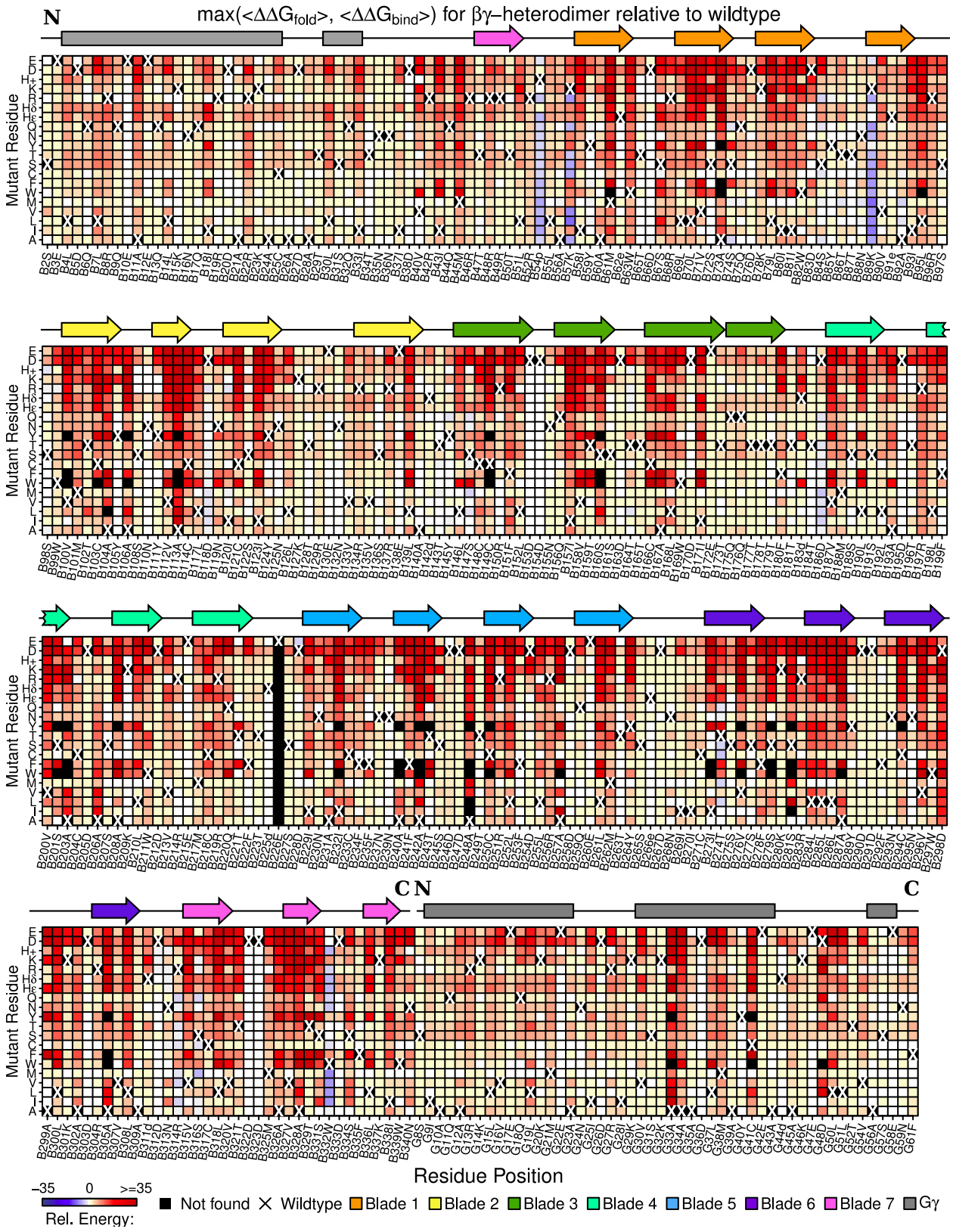

Figure S11: Each value shown is the worst of either stability or binding energy terms, since a functional protein must satisfy both requirements. The majority of mutations are either neutral or unfavorable relative to the wild-type sequence, as seen in yellow and red, respectively.

5 Completeness of computational sampling

Sufficiency of sample size. Including additional backbone conformations for performing DEE/A* is expected to improve the accuracy of our sampling, and these data can show how mutations behave consistently over an ensemble of structures. To determine whether or not a sufficient number of representations were used in our analysis, we considered the average energy difference between sequential subsets of intervals. Only the energy data for stability are considered in this analysis, since variance in binding energy is naturally low due to a small number of positions actually involved in binding. From our data, we defined the following subsets of conformations (**Table S4**):

Table S4: Structures are listed in intervals according to nanosecond in simulation.

A:	[1,5]
B:	[1,5] ∪ [48,52]
C:	[1,5] ∪ [48,52] ∪ [98,102]
D:	[1,5] ∪ [48,52] ∪ [98,102] ∪ [148,152]
E:	[1,5] ∪ [48,52] ∪ [98,102] ∪ [148,152] ∪ [198, 202]
F:	[1,5] ∪ [48,52] ∪ [98,102] ∪ [148,152] ∪ [198, 202] ∪ [248, 252]
G:	[1,5] ∪ [48,52] ∪ [98,102] ∪ [148,152] ∪ [198, 202] ∪ [248, 252] ∪ [298, 302]
H:	[1,5] ∪ [48,52] ∪ [98,102] ∪ [148,152] ∪ [198, 202] ∪ [248, 252] ∪ [298, 302] ∪ [346, 350]

The average energy of each sequence was computed for each subset, and we measured how this average energy will change from one subset to another, in alphabetical order by taking the absolute difference between corresponding sequences: $|\langle A\rangle - \langle B\rangle|$, $|\langle B\rangle - \langle C\rangle|$, $|\langle C\rangle - \langle D\rangle|$, and so forth. The difference in energy variation as the number of structural ensembles increased was partitioned into 1-kcal/mol bins, and the distribution of variance across them is measured to summarize how sampling improves the consistency of our energetic data (**Fig. S12**). We found that including additional snapshots could dramatically reduce the number of outliers in our protein sequence space. In practice, eliminating outliers entirely might not be possible, if flexible regions exist in the protein being studied; it is expected that highly flexible proteins will require more structural conformations for analysis.

Selection of rotamer library. We were interested in seeing how well the augmented Dunbrack–Karplus library ($\pm 10^\circ$ to each χ_1- and χ_2-angle) performed by taking DEE/A* results from a single backbone conformation, and applying a Newton–Rhapson energy minimization algorithm to it (**Fig. S15**). Due to the large energetic calculations and number of residues involved in stability, our analysis only focused on changes in $\Delta\Delta G_{fold}$. As indicated in the main text, approximately 14% of the sequences were found to be unfavorable in one approach and favorable in the other. Unfavorable states remained unfavorable in about 60% of the sequences, while favorable sequences remained favorable in approximately 20% of the data. This indicates that only about 7% of over 6000 sequences could be improved in a meaningful way using energy minimization. Discrepancies in energy calculations tend to arise with the aromatic amino acids, or the charged ones (**Fig. S17**). Most of the energetic improvements that arise from off-rotamer sampling are very modest: the majority of energy differences between the two methods were within 5 kcal/mol of each other, prior to

any adjustment with effective temperature (**Fig. S16**). Furthermore, minimization of the wild-type structure also contributed to energetic discrepancies between the two methods of calculation, by lowering the energy of the reference state.

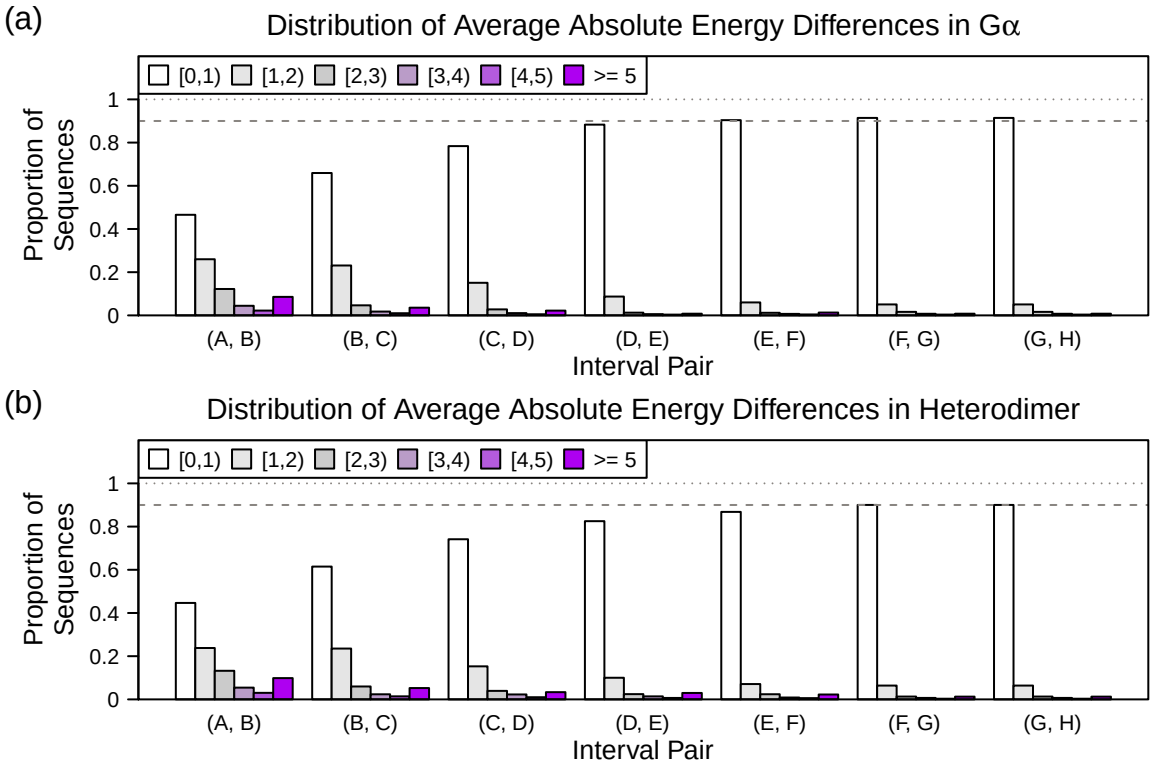

Figure S12: The proportion of data at [0,1)-, [1,2)-, [2,3)-, [3,4)-, [4,5)-kcal/mol or $\geq$ 5-kcal/mol as the number of conformations included in sampling increases (see **Table S4**) is shown. Sequences for Gα and the $\beta\gamma$-heterodimer show similar patterns in convergence, as the number of conformations used to represent an ensemble of states increases.

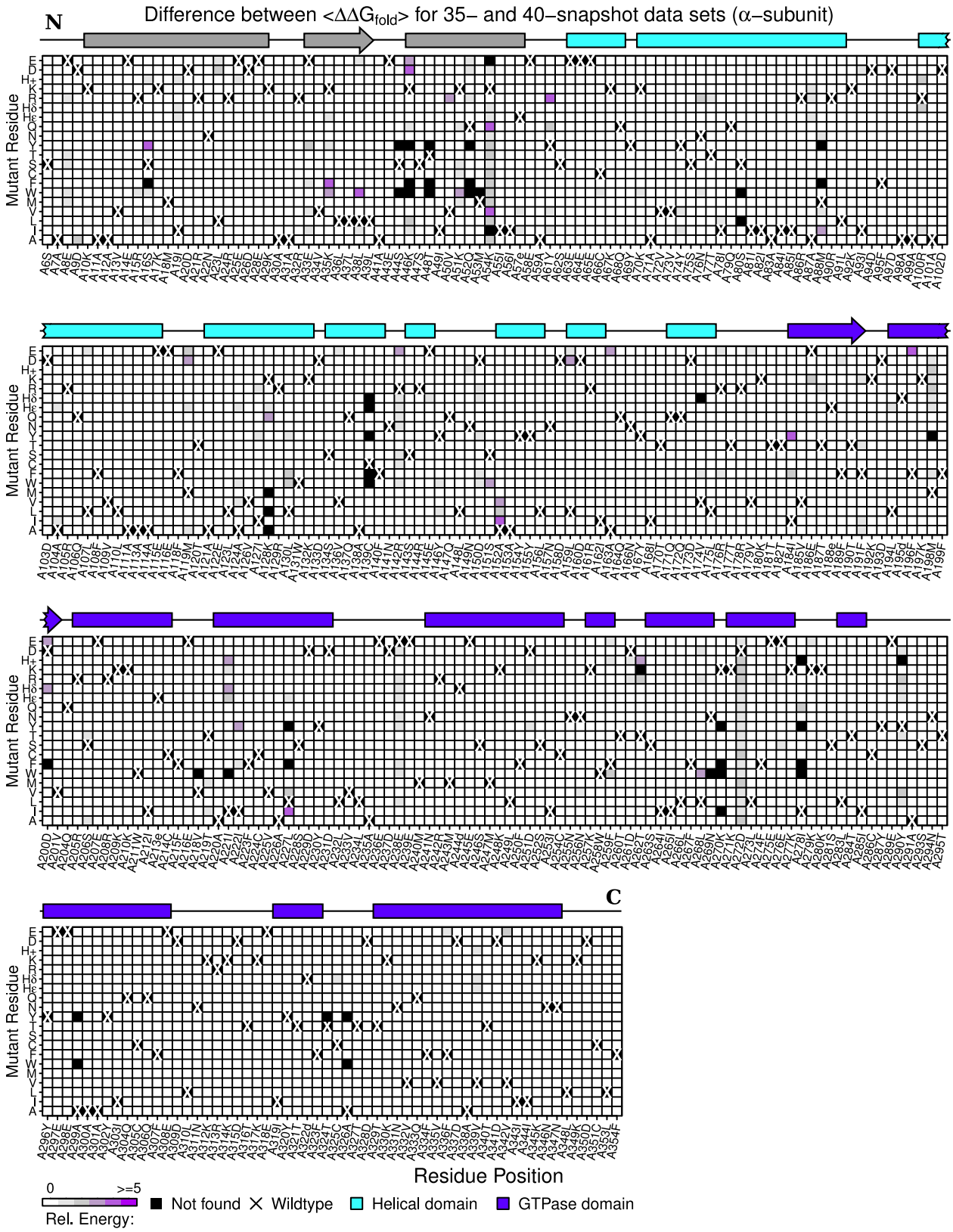

Figure S13: Difference between $\langle \Delta\Delta G_{fold} \rangle$ using a 35- and 40-snapshot data set for Gα is shown here for comparison. Most positions have converged (white and light purple), but there are a few outliers in regions that are harder to sample.

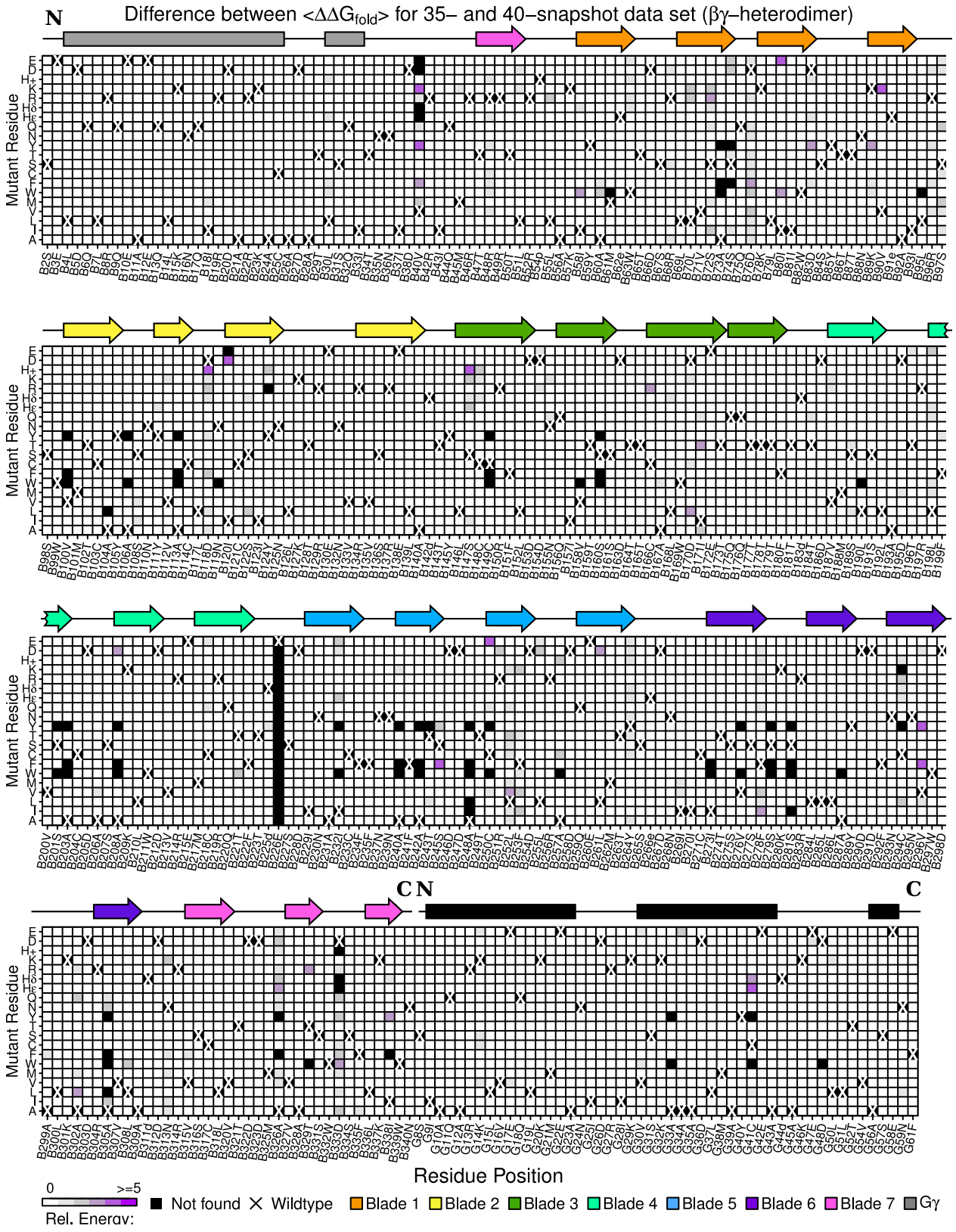

Figure S14: Convergence in the data is found in most of the $\beta\gamma$-heterodimer, shown here as the difference between $\langle \Delta\Delta G_{fold} \rangle$ between a 35- and 40-snapshot data set. Purple regions indicate larger energetic variance, while lighter areas suggest minimal energetic variation.

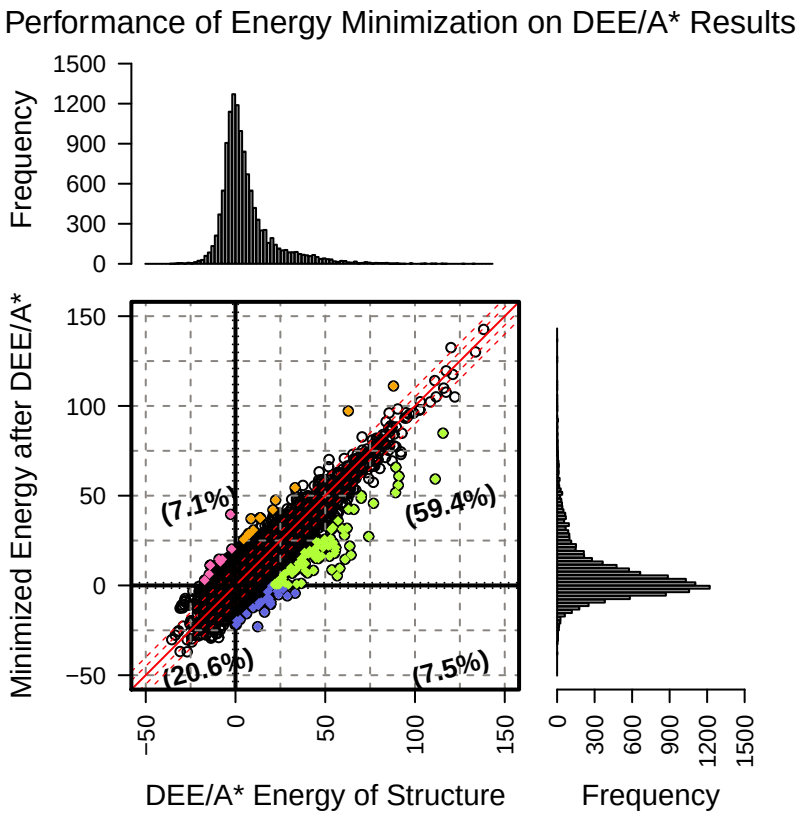

Figure S15: A Newton–Rhapson algorithm was used to perform energy minimization on all DEE/A* structures for one snapshot, to compare the two methods in searching rotamers. The energy landscape is divided into four quadrants to illustrate regions in which energetic improvements can and cannot be achieved when one approach is chosen instead of the other. Red lines indicate where $y = x$, and boundaries that are -10, -5, 5 and 10 kcal/mol from it are shown in dotted red lines.

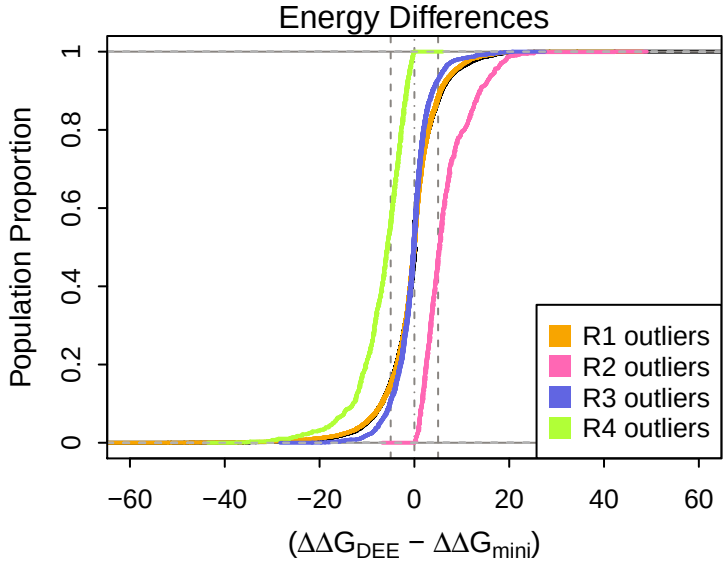

Figure S16: Energy difference between the two protocols was computed for each sequence, and a cumulative distribution of all mutant sequences from a single conformation is shown here, based on this computed difference. Colors correspond to the different quadrants defined previously in **Fig. S15**, and gray lines indicate a difference of -5, 0 or 5 kcal/mol for visual reference.

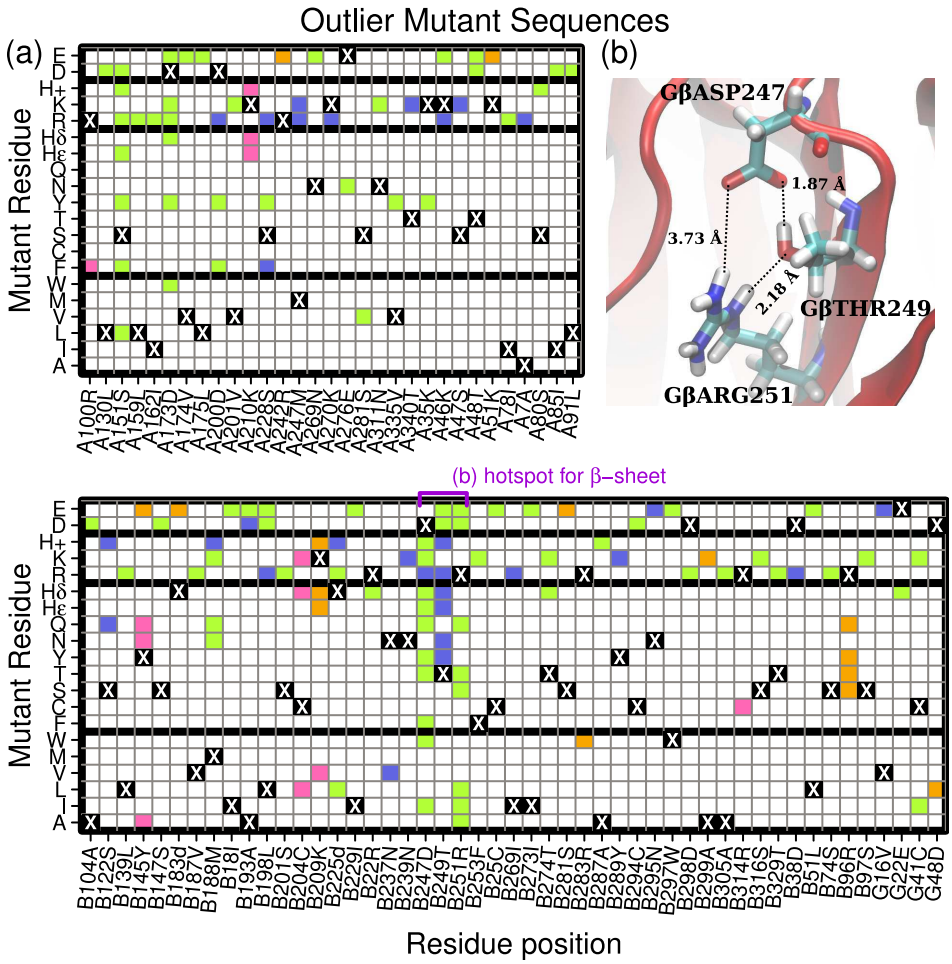

Figure S17: Outlier sequences, those having a 20-kcal/mol difference or greater between the two energy calculation methods, for the four quadrants (defined in **Fig. S15**) are shown and reveal underlying substitutions that yield the greatest discrepancy in (a). An example of a β-sheet with specific side-chain packing requirements that consistently favor wild type is shown in (b).

6 Reflecting evolutionary fitness pressures using DEE/A* approach

Determining frequency of substitution, e_{ij}. Similarity matrices traditionally compute scores as half-bit units. In general, the observed frequencies of amino acid i converted into amino acid j, e_{ij}, is computed, and compared with the expected probabilities of finding each amino acid naturally (p_i and p_j, respectively.) The score, S_{ij}, reflects how closely the observed and theoretical (expected) probability are to each other by taking their ratio (Eq. 1):

$$S_{ij} = 2log_2\frac{e_{ij}}{p_i p_j} \quad \text{(Eq. 1)}$$

For computing e_{ij}, the number of sequences found to satisfy the 1.5 kcal/mol energetic cutoff for both structural stability and binding interactions simultaneously was counted, for each (i, j)-pair of amino acids, and this number was normalized by the total number of sequences satisfying this evolutionary pressure. Meanwhile, the distribution of wild-type amino acids in $G\alpha_{i1}\beta_1\gamma_2$ was used to compute independent probabilities, p_i and p_j (Fig. **S18**). Unlike the standard similarity matrices, wild type and the mutant amino acid that it transitions to is clearly defined in DEE/A*, and thus (i, j)- and (j, i)-pairs are unique; these differences cannot be distinguished in PAM and BLOSUM, and so DEE/A* yields a non-symmetric matrix instead.

By taking wild type as the probability distribution of each amino acid found in $G_i\alpha_1\beta_1\gamma_2$ (e.g. the p_i and p_j terms) we convert PAM and BLOSUM scores into the appropriate e_{ij} terms with these as theoretical probabilities. By rearrangement, the expected frequency of substitution can be expressed as a function of these independent probabilities and the score given by the similarity matrix, (Eq. 2).

$$\begin{aligned} log_2\frac{e_{ij}}{p_i p_j} &= \frac{1}{2}S_{ij} \\ e_{ij} &= p_i p_j 2^{(S_{ij}/2)} \end{aligned} \quad \text{(Eq. 2)}$$

Correlation between DEE/A* with PAM and BLOSUM) A strong correlation exists between the expected values from DEE/A* and those derived starting from PAM or BLOSUM scores. To start, we looked at protein fitness as the sum of structural stability and binding interactions, at different proportions, and found that a uniform contribution from both aspects of fitness optimizes the correlation between the two different approaches of computing e_{ij}, regardless of the similarity matrix being used for comparison, **Fig. S19** and **Fig. S20**. The exact contribution of each term to overall fitness, of course, cannot be determined; regardless of the defined proportions, the comparison between DEE/A* with these similarities matrices outperforms randomly generated data, either from drawing random values within the boundaries of PAM and BLOSUM scores or by shuffling the entries of each respective similarity matrix. Computations are very quick for these random samples, and we have found from 250, 500 and 1000 trials that the Pearson's correlation coefficient remains unchanged (**Fig. S22**, and **Table S5**). The influence of permuting PAM120 or BLOSUM62

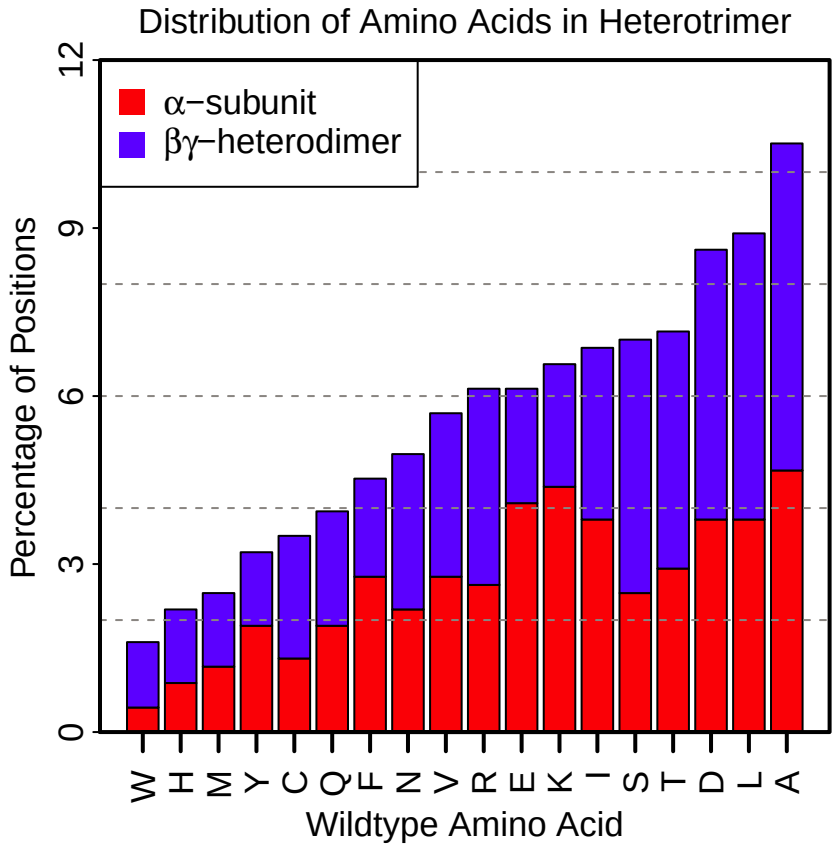

Figure S18: Distribution of wild type amino acids in $G\alpha_{i1}\beta_1\gamma_2$ are normalized and used to provide theoretical probabilities for assessing DEE/A* performance.

is shown by comparing the correlation between the chosen original matrix and the permuted version; a total of 250, 500 and 1000 trials were performed, and the correlation between these two sets of matrices is consistent ($\rho^2 \approx 0.7$ or 0.8 for PAM120 and BLOSUM62, respectively.) Furthermore, while some correlation between DEE/A* and the permuted matrices exist, this relationship is strongest when the (i, j) pairs are clearly identified, suggesting that DEE/A* can discriminate between amino acids well (**Fig. S21**).

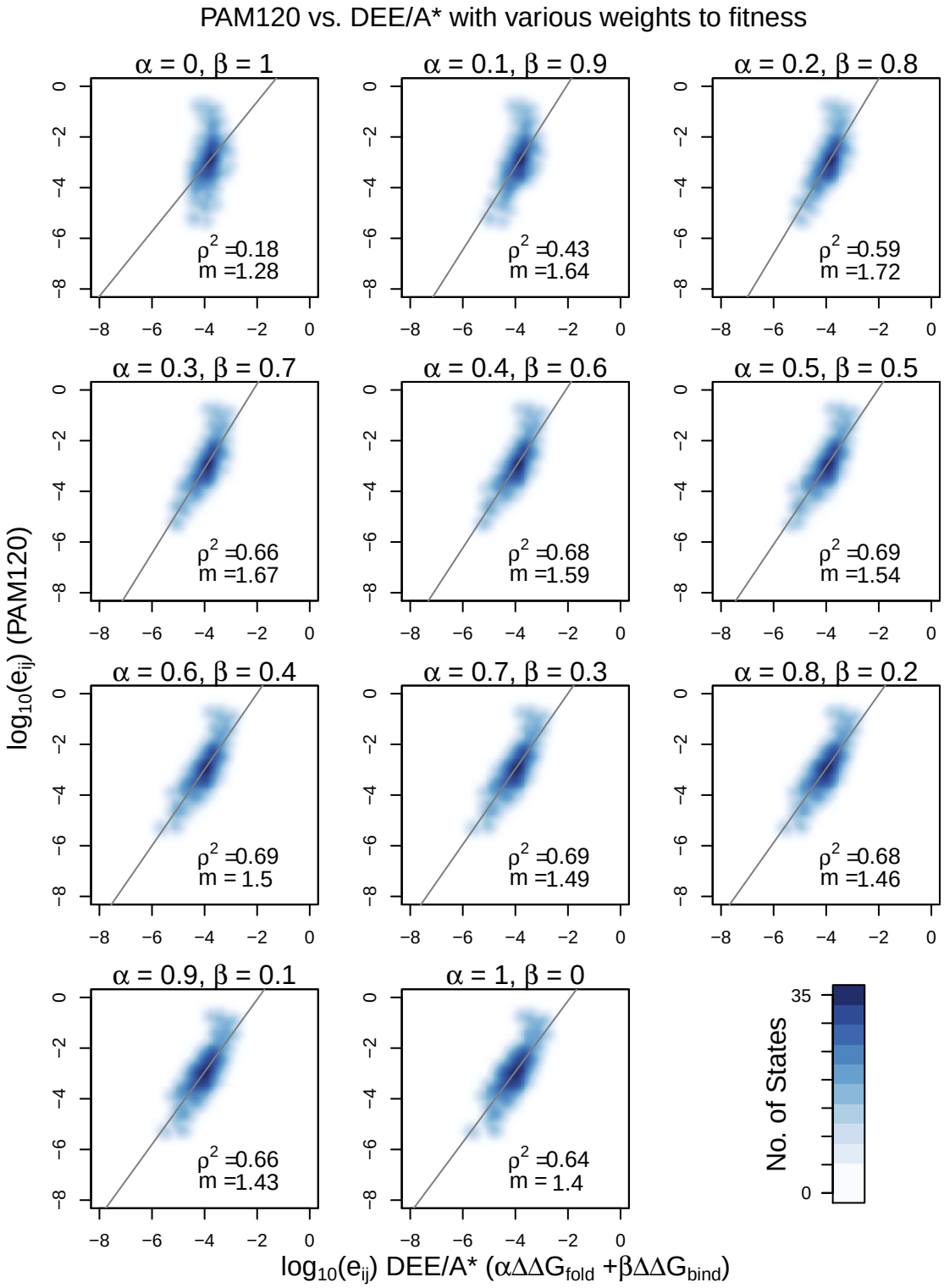

Figure S19: Different proportions of stability and binding were used to define the energetic criteria for survival. Correlation between the expected rate of substitution of amino acid i with j, e_{ij}, is compared between PAM120 and DEE/A* data. Pearson's correlation coefficient and the slope of the least-squares fit are included. The best-fit line is shown in black.

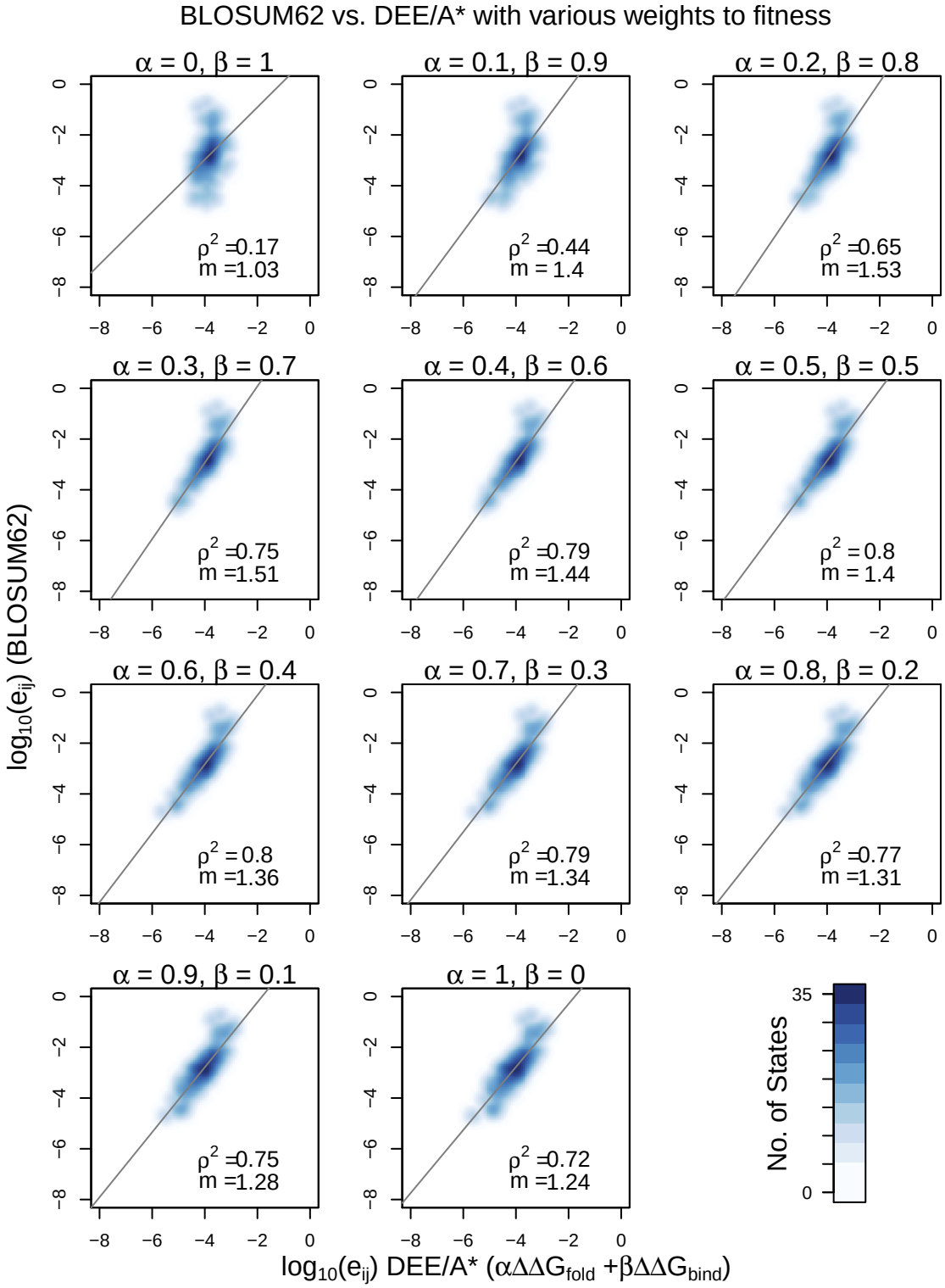

Figure S20: Starting with BLOSUM62 scores, the expected frequency of finding amino acid i replacing j, e_{ij}, was calculated with DEE/A* data, for different combinations of energy contribution from stability and binding interactions. Analogous values were computed from BLOSUM62, so that the two sets of substitution rates can be compared. Pearson's correlation coefficient as well as the slope of the least-squares fit is shown for each; the best-fit line is also drawn.

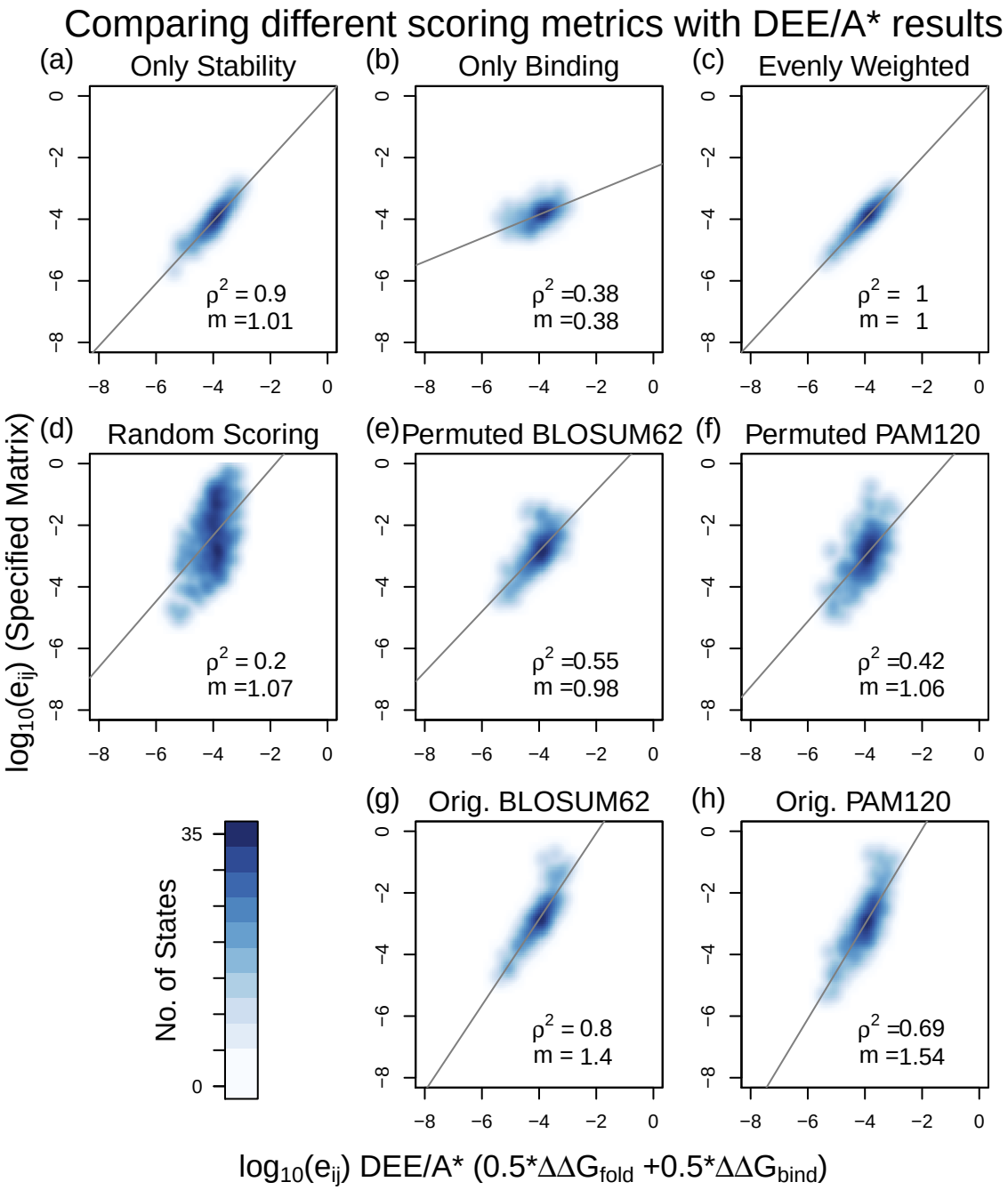

Figure S21: Assuming a uniform contribution from stability and binding, expected frequencies of substitution, e_{ij}, were compared to (from left to right) scores: (a) accounting only for stability; (b) accounting only for binding; (c) in which stability and binding are evenly weighted (50–50); (d) generated from a uniform distribution, bounded by $\max(BLOSUM62, PAM120)$ (e) permuted BLOSUM62 matrix; (f) permuted PAM120 matrix; (g) original BLOSUM62 matrix; and (h) original PAM120 matrix.

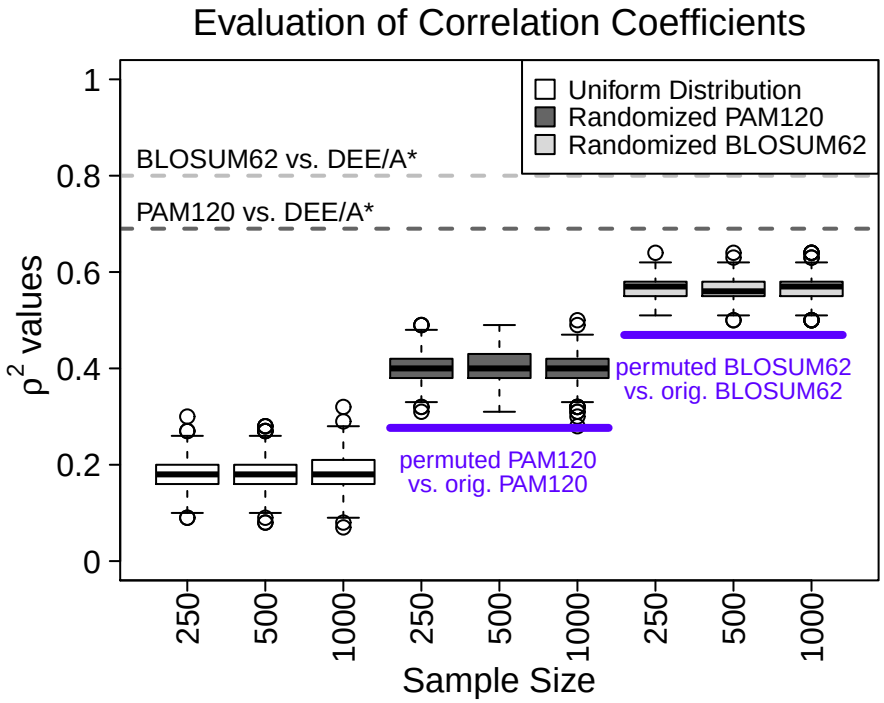

Figure S22: The Pearson's correlation coefficient between DEE/A* data (with 50–50 distribution between stability and binding interactions) and permuted matrix from either a random distribution (white), PAM120 (gray) or BLOSUM62 (light gray) was computed for samples of size $n = 250, 500$ and 1000. Distributions are generally consistent within each family of distributions. Dotted lines indicate the correlation measured between the original PAM120 (gray) or BLOSUM62 (light gray) with DEE/A* based on a 50–50 contribution from each aspect of fitness, as seen in **Fig. S19** and **Fig. S20**. Solid, indigo lines indicate the correlation between either PAM120 or BLOSUM62 with the permuted version of itself.

Table S5: Average Pearson's correlation coefficient between DEE/A* and randomly generated data for various sample sizes. Number of samples given by n.

Randomized matrix	$n = 250$	$n = 500$	$n = 1000$
Uniform distribution	0.18 ± 0.03	0.18 ± 0.04	0.18 ± 0.04
PAM120 values	0.40 ± 0.03	0.40 ± 0.03	0.40 ± 0.03
BLOSUM62 values	0.57 ± 0.02	0.56 ± 0.02	0.57 ± 0.02

Table S6: Average Pearson's correlation coefficient between original similarity matrix and the permuted version. Number of samples given by n.

Similarity matrix	$n = 250$	$n = 500$	$n = 1000$
PAM120	0.27 ± 0.03	0.28 ± 0.03	0.28 ± 0.03
BLOSUM62	0.46 ± 0.03	0.47 ± 0.03	0.47 ± 0.03

7 Comparisons with established experimental data

Alanine scan of Gα. A full-scale alanine scan was performed by Sun, *et al.* for Gα in which thermal stability was measured relative to wild type (ΔT_m) for all single mutants. The corresponding alanine mutations from our DEE/A* were used for comparison to these data. In our analysis, a positive outcome was defined as a mutation that was destabilizing relative to wild type ($\Delta\Delta G_{fold} > +1.5$ kcal/mol), which would suggest that native interactions were important for structural stability. We quantified the proportion of

- true positives ($\Delta\Delta G_{fold} > 1.5$ kcal/mol & $\Delta T_m \leq -2^{\circ}C$)
- true negatives ($\Delta\Delta G_{fold} \leq 1.5$ kcal/mol & $\Delta T_m > -2^{\circ}C$)
- false positives ($\Delta\Delta G_{fold} > 1.5$ kcal/mol & $\Delta T_m \leq -2^{\circ}C$) and
- false negatives ($\Delta\Delta G_{fold} \leq 1.5$ kcal/mol & $\Delta T_m > -2^{\circ}C$)

The relationship between thermal stability and our DEE/A* calculations is illustrated in **Figure S23**, and we report additional statistics in **Table S7**. To provide a basis for comparing these proportions, the mutation free energy for DEE/A* and thermal stability were randomized for a total of 5000 independent trials, then compared again to measure the proportion of different outcomes (**Table S7** & **Fig. S24**). We found that the observed number of correctly identified outcomes (true positives and true negatives) were consistently higher than expected, and that the proportion of incorrect predictions (false positives and false negatives) were consequently much lower. These results were further quantified in terms of sensitivity and specificity (**Table S8**), and we found that sensitivity was much higher than the randomized energy data. Here, there is a natural trade-off with specificity, which was found to be relatively lower in comparison to the shuffled energy values.

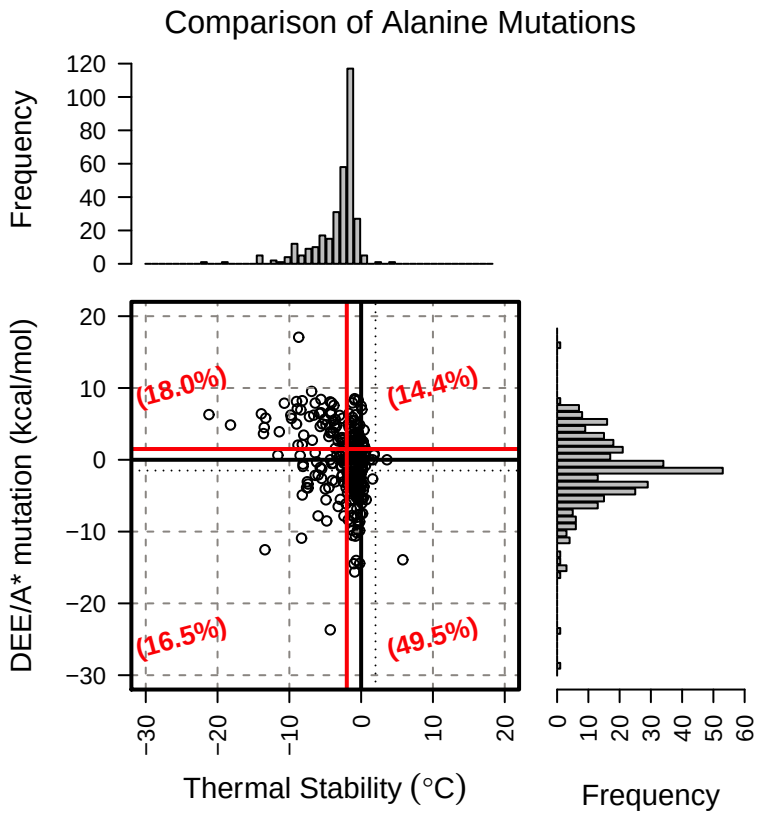

Figure S23: The energetic difference between each wild-type residue and corresponding alanine mutation in the stability of $G\alpha$–GDP are shown here. The thermal stability (ΔT_m) between alanine mutations and wild type measured by Sun, *et al.* were used for comparison with the alanine mutants from our DEE/A* computations for structural stability. The red vertical lines correspond to $-2^{\circ}C$, the threshold used by Sun, *et al.* to indicate that native interactions were important in stabilizing $G\alpha$–GDP, while the red horizontal line is the cutoff used in our calculations to indicate that a substitution is unfavorable relative to the wild-type residue. These red lines are used to define the four different quadrants, and the percentage in each region is shown in red text within parentheses. (See also **Fig. S7**.)

Table S7: Correlation between alanine mutants for DEE/A* calculations and thermal stability data measured by Sun, *et al.* was quantified by the proportions of true positives, false positives, true negatives and false negatives. The sensitivity and specificity of our computational approach were also calculated. (See also **Fig. S23**.)

		DEE/A* calculations	
		$\Delta\Delta G_{fold} > +1.5$ kcal/mol	$\Delta\Delta G_{fold} \leq 1.5$ kcal/mol
Thermal Stability	$\Delta T_m \leq -2^{\circ}C$	18.0% ($n = 59$)	14.4% ($n = 47$)
	$\Delta T_m > -2^{\circ}C$	16.5% ($n = 54$)	49.5% ($n = 162$)
		Sensitivity: 0.52	Specificity: 0.78

Table S8: After randomizing the DEE/A* alanine mutants, the proportion of true positives, false positives, false negatives and true negatives were measured. The reported values are the average and standard deviations for each category after 5000 independent calculations. The sensitivity and specificity have also been measured. (See also **Fig. S24**.)

		DEE/A* calculations (randomized)	
		$\Delta\Delta G_{fold} > +1.5$ kcal/mol	$\Delta\Delta G_{fold} \leq 1.5$ kcal/mol
Thermal Stability	$\Delta T_m \leq -2°C$	$11.0 \pm 1.2\%$	$21.4 \pm 1.2\%$
	$\Delta T_m > -2°C$	$23.1 \pm 1.2\%$	$42.8 \pm 1.2\%$
		Sensitivity: 0.32 ± 0.04	Specificity: 0.67 ± 0.02

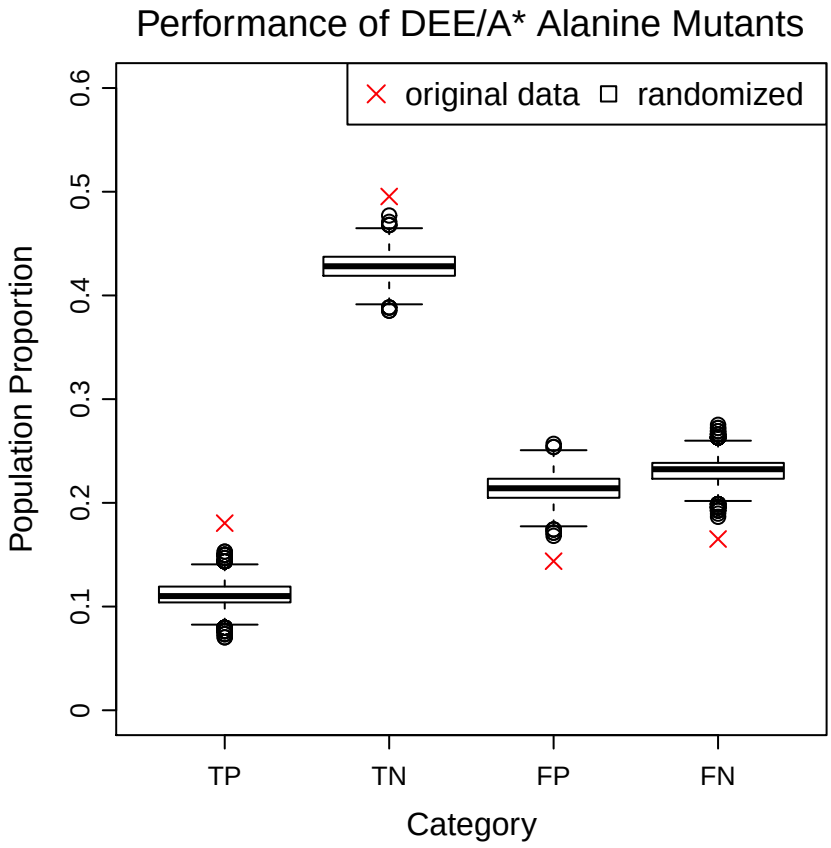

Figure S24: The proportions of different true positive, true negative, false positive and false negative outcomes were calculated, and the distribution of these values from randomized data are shown using box-and-whiskers for each outcome type. Red X's are included to represent the computed values of each category from the initial comparison of DEE/A* and thermal stability.

Oncogenic point mutations in Gβ. The original list of point mutations was provided by Yoda, *et al.* in the supplementary information of their publication. This included a few mutations that were not suitable for comparison, such as mutations to glycine or using splice variants, which are not covered by our computational protocol, and thus excluded from analysis. Mutations to histidine were taken as the average mutation free energy of all three possible histidine states (δ-, ε- and doubly-protonated) as modeled by CHARMM. A total of 36 point mutations were available for analysis, and are listed in **Table S9**. From our DEE/A* calculations for each point mutation listed, the stability and binding interactions relative to wild type were used to categorize mutations as gain-of-function, neutral or loss-of-function. These energetic cutoffs were based on previous definitions using $\pm$1.5 kcal/mol. Mutations were assessed as independent aspects of fitness, and also simultaneously. For the latter, we measured the maximum magnitude of either structural stability or binding interactions. (See main text.)

Table S9: The original list of GNB1 mutations was compiled and amended by Yoda, *et al.* A condensed version of point mutations that could be compared to our DEE/A* data (*e.g.* not a glycine mutation, splice variant or non-specific mutation) is provided here, along with the computed DEE/A* values for Gβ structural stability ($\Delta\Delta G_{fold}$) and binding interactions ($\Delta\Delta G_{bind}$). References may be from Yoda, *et al.*, COSMIC, cBioPortal or a specific publication, in which the PubMed identification number is provided.

Mutation	$\Delta\Delta G_{fold}$	$\Delta\Delta G_{bind}$	References	Mutation	$\Delta\Delta G_{fold}$	$\Delta\Delta G_{bind}$	References
A11V	−4.0	0.0	COSMIC	D118Y	−7.3	−7.9	COSMIC
R19L	−11.5	0.0	COSMIC	S147A	−14.7	−3.2	Yoda, *et al.*
A21S	2.1	0.0	COSMIC	B177K	−10	0.0	24220272
Q32K	0.6	0.0	COSMIC	S191C	−13	0.0	COSMIC
T47M	−11.6	0.0	COSMIC	D205N	−14.7	0.5	COSMIC
p54N	−16.8	−17.0	COSMIC	E215D	−5.9	0.0	cBioPortal
K57E	−1.2	4.3	Yoda, *et al.*	d225L	−24.3	−0.1	23292937
			COSMIC	D228N	−17.9	−7.1	cBioPortal
L57E	−1.2	4.3	Yoda, *et al.*	N230S	−4.4	−11.0	COSMIC
			COSMIC	R256H	5.1	5.1	cBioPortal
			24220272	D258N	−25.4	0.0	COSMIC
			23443460	E260K	−9.8	0.0	COSMIC
K57N	−8.4	−2.2	23443460	M262T	2.8	0.0	COSMIC
K57T	−2.7	−1.9	COSMIC	I269T	−22.4	0.0	COSMIC
K78E	−4.0	0.3	COSMIC	K280N	−5.8	0.0	cBioPortal
			cBioPortal	S281N	−1.1	0.0	COSMIC
K78Q	−10.0	−3.7	Yoda, *et al.*	R283C	−15.5	0.0	COSMIC
I80N	−3.8	−1.8	Yoda, *et al.*	R314H	−5.3	−5.3	23699601
			22343534	A326T	4.8	0.0	cBioPortal
I80T	2.5	−11.1	Yoda, *et al.*				
			COSMIC				
			23699601				
			24220272				
N88D	2.4	−18.1	Yoda, *et al.*				
K89E	−17.9	−17.1	Yoda, *et al.*				
K89T	−20.5	−20.6	24220272				
R96H	0.4	−0.4	COSMIC				

8 Statistical analysis for predictions

The Boltzmann-weighted mean of each mutant sequence was computed to determine the average change in all 40 structural states used. For each position, this provided twenty unique values (one for each amino acid) which summarized all mutational effects. From this vector of numbers, values on the $[-1.5, 1.5]$-kcal/mol interval were assigned zero to represent no change. A 20-dimensional zero vector was thus chosen for the null hypothesis, and the Mann–Whitney–Wilcoxon test was performed using R for every position in the heterotrimer. Computed p-values are shown in **Fig. S25** and grouped according to (1) whether or not position is known to have binding interactions (according to Wall, *et al.*) and (2) whether mutation free energy is based on $\Delta\Delta G_{fold}$ or $\Delta\Delta G_{bind}$.

The findings for data based on binding interactions are discussed in the main text. A detailed list for true positives, false negatives and predicted positions can be found in **Tables S10 & S11**. The calculations for stabilizing interactions, however, suggest that nearly all positions have a meaningful contribution to protein tertiary structure (low p-values). Given that this protein family is highly evolved and that the mutational profiles (**Fig. S5–S11**) suggested that most substitutions are unfavorable, alternative metrics would need to be applied to further separate side chains into varying degrees of involvement.

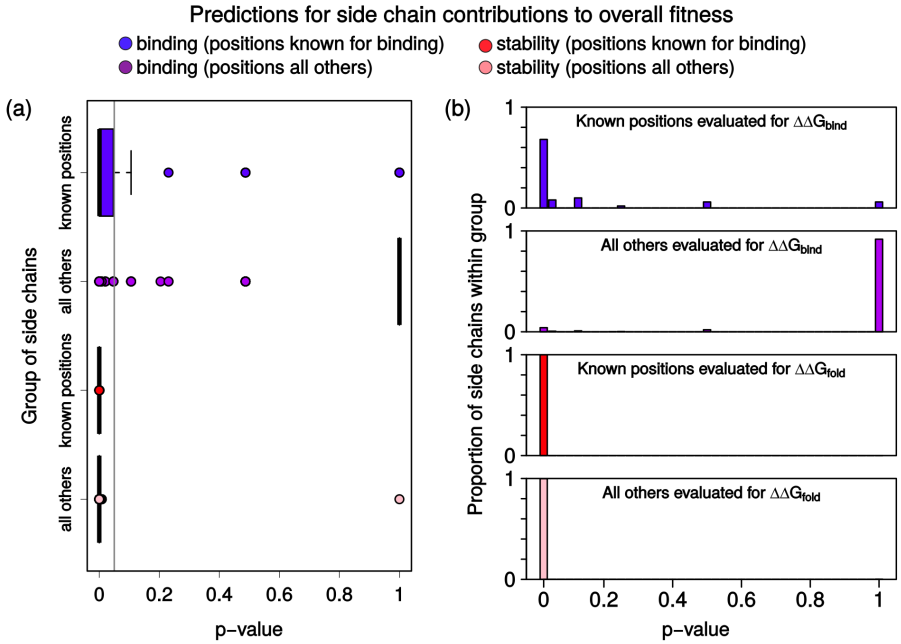

Figure S25: Positions known for binding interactions were separated from all other positions, then mutational differences based on $\Delta\Delta G_{bind}$ and $\Delta\Delta G_{fold}$ were computed (blue and red, respectively.) The analysis was applied to all other positions based on $\Delta\Delta G_{bind}$ and $\Delta\Delta G_{fold}$ (purple and pink, respectively) for comparison. These data are shown as distributions in (a) box-and-whiskers plots and (b) as a histogram to illustrate how the majority of side chains within each subgroup shifts as the premise for analysis changes.

Table S10: The positions known to have binding interactions according to Wall, *et al.* are provided here. The computed p-values are the untruncated output from R and based on $\Delta\Delta G_{bind}$ energetic differences from wild type.

Position	p-value	Position	p-value
A12A	1.453066e-04	B52R	3.046867e-10
A13V	0.4871795	B55L	3.276003e-03
A15R	1.541715e-07	B57K	3.046867e-10
A16S	4.509515e-05	B59Y	4.712405e-02
A19I	1.288433e-05	B75Q	2.019602e-02
A20D	3.351553e-09	B78K	3.046867e-10
A23L	4.359198e-04	B80I	1.288433e-05
A24R	0.4871795	B88N	2.019602e-02
A26D	4.509515e-05	B89K	3.046867e-10
A182T	0.1060291	B90V	0.1060291
A184I	4.359198e-04	B91e	4.712405e-02
A186E	3.351553e-09	B99W	7.708573e-07
A199F	4.712405e-02	B101M	0.1060291
A204Q	4.359198e-04	B117L	2.569524e-08
A206S	4.359198e-04	B119N	1.453066e-04
A207E	2.569524e-08	B132N	1.0000000
A209K	0.2307692	B143T	1.0000000
A210K	1.453066e-04	B145Y	2.019602e-02
A211W	1.228501e-03	B186D	3.276003e-03
A213e	4.509515e-05	B188M	0.4871795
A214C	3.276003e-03	B204C	4.359198e-04
A215F	0.1060291	B228D	0.1060291
A216E	8.316008e-03	B230N	4.712405e-02
A258W	3.046867e-10	B246D	3.276003e-03
		B332W	3.340382e-06

Table S11: Using $\Delta\Delta G_{bind}$ data, these positions were predicted to be at the binding interfaces of the heterotrimer. Values are untruncated R output.

Position	p-value	Position	p-value
A6S	3.276003e-03	B54p	2.569524e-08
A8E	1.288433e-05	B56A	2.019602e-02
A9D	2.569524e-08	B68R	3.351553e-09
A17K	2.019602e-02	B74S	3.276003e-03
A21R	2.569524e-08	B76D	2.019602e-02
A29K	4.712405e-02	B83D	4.712405e-02
A30A	8.316008e-03	B84S	4.359198e-04
A35K	3.340382e-06	B85Y	4.712405e-02
A197K	3.276003e-03	B86T	4.359198e-04
A218V	4.359198e-04	B92A	1.453066e-04
		B97S	1.453066e-04
		B98S	4.712405e-02
		B118D	7.708573e-07
		B120I	8.316008e-03
		B129R	1.288433e-05
		B147S	4.509515e-05
		B274T	1.453066e-04
		B313N	1.228501e-03
		B314R	7.708573e-07
		B316S	1.453066e-04